Awake responses suggest inefficient dense coding in the mouse retina

Authors: Tom Boissonnet[1,2,3], Matteo Tripodi[1], Hiroki Asari*[1]

Affiliations:

1. Epigenetics and Neurobiology Unit, EMBL Rome, European Molecular Biology Laboratory, Monterotondo, 00015, Italy

2. Collaboration for joint PhD degree between EMBL and Université Grenoble Alpes, Grenoble Institut des Neurosciences, La Tronche, 38700, France

3. Current address: Center for Advanced Imaging, Heinrich-Heine-Universität Düsseldorf, Düsseldorf, 40225, Germany.

***Corresponding author:** Hiroki Asari, E-mail: asari@embl.it

Author contributions: T.B. and H.A. designed the study; T.B. and M.T. performed experiments; T.B., M.T. and H.A. analyzed the results; and T.B., M.T. and H.A. wrote the manuscript.

Competing interests: The authors declare no competing financial interests.

Key words: retinal ganglion cells; in vivo recordings; awake; anesthesia; efficient coding.

Acronyms: CMOS, complementary metal-oxide semiconductor; DS, direction-selectivity; dLGN, dorsal lateral geniculate nucleus; DLP, digital light processing; FMM, fentanyl, medetomidine and midazolam; GABA, gamma-aminobutyric acid; LED, light emitting diode; OS, orientation-selectivity; OT, optic tract; PCA, principal component analysis; PFA, paraformaldehyde; RGC, retinal ganglion cells; SC, superior colliculus; STA, spike-triggered average; UV, ultraviolet.

Abstract

The structure and function of the vertebrate retina have been extensively studied across species with an isolated, *ex vivo* preparation. Retinal function *in vivo*, however, remains elusive, especially in awake animals. Here we performed single-unit extracellular recordings in the optic tract of head-fixed mice to compare the output of awake, anesthetized, and *ex vivo* retinas. While the visual response properties were overall similar across conditions, we found that awake retinal output had in general 1) faster kinetics with less variability in the response latencies; 2) a larger dynamic range; and 3) higher firing activity, by ~20 Hz on average, for both baseline and visually evoked responses. Our modeling analyses further showed that such awake response patterns convey comparable total information but less efficiently, and allow for a linear population decoder to perform significantly better than the anesthetized or *ex vivo* responses. These results highlight distinct retinal behavior in awake states, in particular suggesting that the retina employs dense coding *in vivo*, rather than sparse efficient coding as has been often assumed from *ex vivo* studies.

Introduction

The vertebrate retina is one of the best characterized parts of the central nervous system (Gollisch and Meister, 2010; Masland, 2012). It consists of ~100 cell types in total (Shekhar et al., 2016; Yan et al., 2020), including ~30 types of retinal ganglion cells (RGCs) that send the retinal output signals to the brain via the optic nerve (Sanes and Masland, 2015; Baden et al., 2016). Each of these RGC types forms distinct neural circuits within the retina to extract specific features of the visual image coming into the eye, such as color, contrast, and motion. The retina thus performs parallel and dynamic processing as the first stage of the visual pathway.

Most of our knowledge on retinal function has been obtained from *ex vivo* studies because isolated retinal tissues are nevertheless functional, i.e., responsive to light (Barlow et al., 1964). While powerful, however, *ex vivo* physiological approaches have certain limitations.

First, one cannot perform long-term recordings (Meister et al., 1994). Second, one cannot avoid artifacts due to retinal dissection, such as the effect of cutting RGC axons (Vidal-Sanz et al., 2017) or retinal epithelial detachment (Strauss, 2005). Neuromodulatory effects of retinopetal pathways are also difficult to study in an isolated retinal preparation (Repérant et al., 2006; Esposti et al., 2013). *In vivo* studies are thus indispensable for understanding to what degrees our knowledge on the retina can be translated from *ex vivo* to fully physiological *in vivo* conditions and clarifying retinal function thoroughly.

Previous physiological studies on the retina *in vivo* were conducted mostly under anesthetized—and often paralyzed—conditions. To monitor RGC activity *in vivo*, for example, single-unit recordings were made directly from the retina (Kuffler, 1953), at the optic nerve or tract fibers (Hartline, 1938; Lettvin et al., 1959; Enroth-Cugell and Robson, 1966; Mastronarde, 1983, 1985; Sagdullaev and McCall, 2005), or in the form of “slow-potential” in the dorsal lateral geniculate nucleus (dLGN; Bishop et al., 1962; Kaplan and Shapley, 1984). Optical methods were also developed to image the activity of retinal neurons directly through the pupil of a live animal under anesthesia (Geng et al., 2012; Yin et al., 2013, 2014). In contrast, thus far only a handful of studies have reported awake recordings from the retina (Esposti et al., 2013; Hong et al., 2018) or its outputs (Weyand, 2007; Liang et al., 2018, 2020; Schröder et al., 2020; Sibille et al., 2022). Thus, despite a long history of research on the retina, it still remains unclear what exactly the eye tells the brain in awake animals.

As recordings from awake behaving animals became routine for many brain areas (Dombeck et al., 2007; Jun et al., 2017), growing attention has been paid to the roles of an animal’s behavior and internal brain states in the function of the sensory systems (Niell and Stryker, 2010; Lee and Dan, 2012). For example, systematic studies on the early visual pathway showed higher firing activity and faster response dynamics in both dLGN (Durand et al., 2016) and the superior colliculus (SC; De Franceschi and Solomon, 2018) of awake animals than those under anesthesia. A critical question that was left unanswered is to what extent such differences originate in the retina.

To clarify differences in the retinal visual response properties between awake and anesthetized conditions, here we employed single-unit extracellular recording techniques from head-fixed mice. Specifically, the electrodes were placed in the optic tract (OT), a bundle of nerve fibers composed of RGC axons as they project from the eye to their main targets: dLGN and SC (Ellis et al., 2016; Rosón et al., 2019). These recordings are superior to direct *in vivo* retinal recordings (e.g., with epiretinally implanted mesh electrodes; Hong et al., 2018) because the retinal circuits and the eye optics remain intact, and also to those extracellular recordings in SC (Sibille et al., 2022) or dLGN (Weyand, 2007) because RGC axonal signals do not need to be disambiguated from those of local axons or somata. This advantage also exists for calcium imaging recordings of the retina directly in the eye of immobilized zebrafish larvae (Esposti et al., 2013) or those of RGC axon terminals in dLGN (Liang et al., 2018, 2020) or SC (Schröder et al., 2020; Molotkov et al., 2022). These imaging approaches, however, lack the temporal precision as in the electrophysiology, which is an important aspect of the information processing in the retina (Gollisch and Meister, 2008).

From our OT recordings, we examined the visual responses to a set of visual stimuli widely used for probing retinal function *ex vivo* (Baden et al., 2016; Jouty et al., 2018), including moving gratings, white-noise stimuli, and full-field flickering stimuli at different temporal frequencies. We used two different anesthetics that are commonly used in neuroscience research: isoflurane gas and an intraperitoneal combination of fentanyl, medetomidine and midazolam (FMM). In both cases, we found that the temporal dynamics of the retinal outputs were slower than in awake recordings, consistent with the previous studies on the effects of anesthesia in retinorecipient areas (dLGN, Durand et al., 2016; SC, De Franceschi and Solomon, 2018). We also found that the retinal outputs in an awake condition had higher baseline firing rates and a larger dynamic range than in anesthetized or *ex vivo* conditions. Consequently, while information was conveyed at a comparable rate in bits per second, the amount of information per spike was lower in the awake responses. Furthermore, we found that a linear decoder performed significantly better with awake population responses.

Thus, our results do not support sparse efficient coding (Attneave, 1954; Barlow and Rosenblith, 1961) or minimum energy principles (Laughlin, 2001) that have been used as a model of the early visual processing (Atick and Redlich, 1990; Gjorgjieva et al., 2019; but see Schwartz, 2021). We instead suggest that the retina may employ dense coding principles *in vivo*.

Results

Characterization of retinal output responses *in vivo*

To monitor retinal output *in vivo*, we established extracellular single-unit recording methods from axons of retinal ganglion cells (RGCs) in the optic tract (OT) of head-fixed mice (Figure 1). In total, we made 17 chronic (75 cells) and 80 acute recordings (207 cells without anesthesia; 325 cells with isoflurane; 103 cells with FMM), where a standardized set of visual stimuli were presented to the subject animal to characterize the visual response properties of the recorded cells (for ~1 hour; Figure 1A,B; see Methods for details). Isolated units typically had a triphasic spike waveform (e.g., Figure 1F-H) as expected from axonal signals (Barry, 2015); and most of them had a minimum interspike interval above 2 ms (e.g., Figure 1I-K; 93%, awake; 94%, isoflurane; 99%, FMM). Histological verification of the electrode location (e.g., Figure 1E) further ensured a successful optic tract recording *in vivo*.

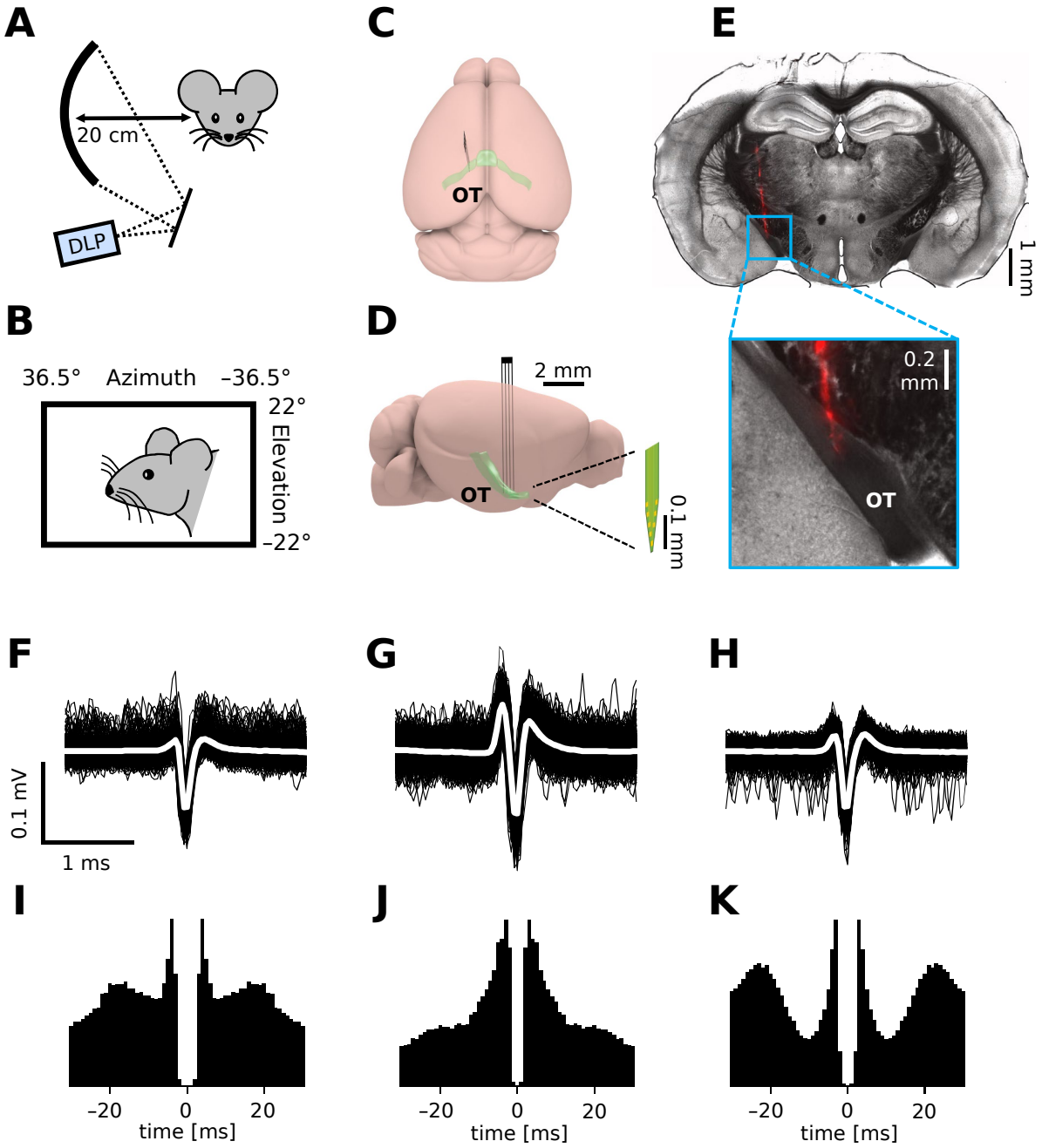

Figure 1: *in vivo* extracellular recordings from the mouse optic tract. *A,B*: Schematic diagram of the experimental set-up. We presented visual stimuli to a head-fixed mouse using a digital light processing (DLP) device projecting images onto a spherical screen placed laterally to the subject animal (A, front-view; B, side-view). See Methods for details and specifications. *C,D*: Schematic diagram (C, top-view; D, side-view) of the brain and electrode location to target the optic tract (OT). *E*: Histological image of a representative brain sample (coronal section, 150 µm thick) showing the electrode trace (red, DiI stain deposited on the electrode). F-K: Spike waveform (F-H; black, individual trials; white, mean) and autocorrelogram (I-K; bin size, 1 ms) for three representative units recorded from the optic tract of an awake mouse.

We performed physiological classification of the recorded cells (Figure 2; see Methods for details). Specifically, we first identified reliably responsive cells based on the visual responses to full-field contrast-inverting stimuli (Figure 2A,B), and categorized their response polarity into ON, ON/OFF, OFF types (Figure 2C). In both anesthetized and awake conditions, we found around 20-50% of ON cells, 10-40% of ON/OFF cells, and 20% of OFF cells in our data sets. We then further classified the cells from the viewpoint of orientation selectivity (OS) and motion-direction selectivity (DS), based on the responses to moving gratings in eight different directions (Figure 2D-F). In the anesthetized conditions, about a half of the cells (42-54%) were either OS or DS or both regardless of their response polarities or anesthetics. This is consistent with a previous *in vivo* study (Hong et al., 2018), but rather higher than one would expect from anatomical and physiological studies *ex vivo* (about a third; Sanes and Masland, 2015; Baden et al., 2016; Jouty et al., 2018). In contrast, we found much less DS/OS cells (17%) in the awake condition. This discrepancy in the fraction of DS/OS cells cannot be explained by a sampling bias *per se*, if any, because we used the same experimental set up between the anesthetized and awake recordings. Instead, it likely arose from a difference in the baseline firing rate (see below and Figure 3). Since DS/OS index is defined as a normalized population vector (Eq.(3). In Methods; Mazurek et al., 2014), higher firing in the awake condition generally leads to a larger denominator, hence a lower DS/OS index value.

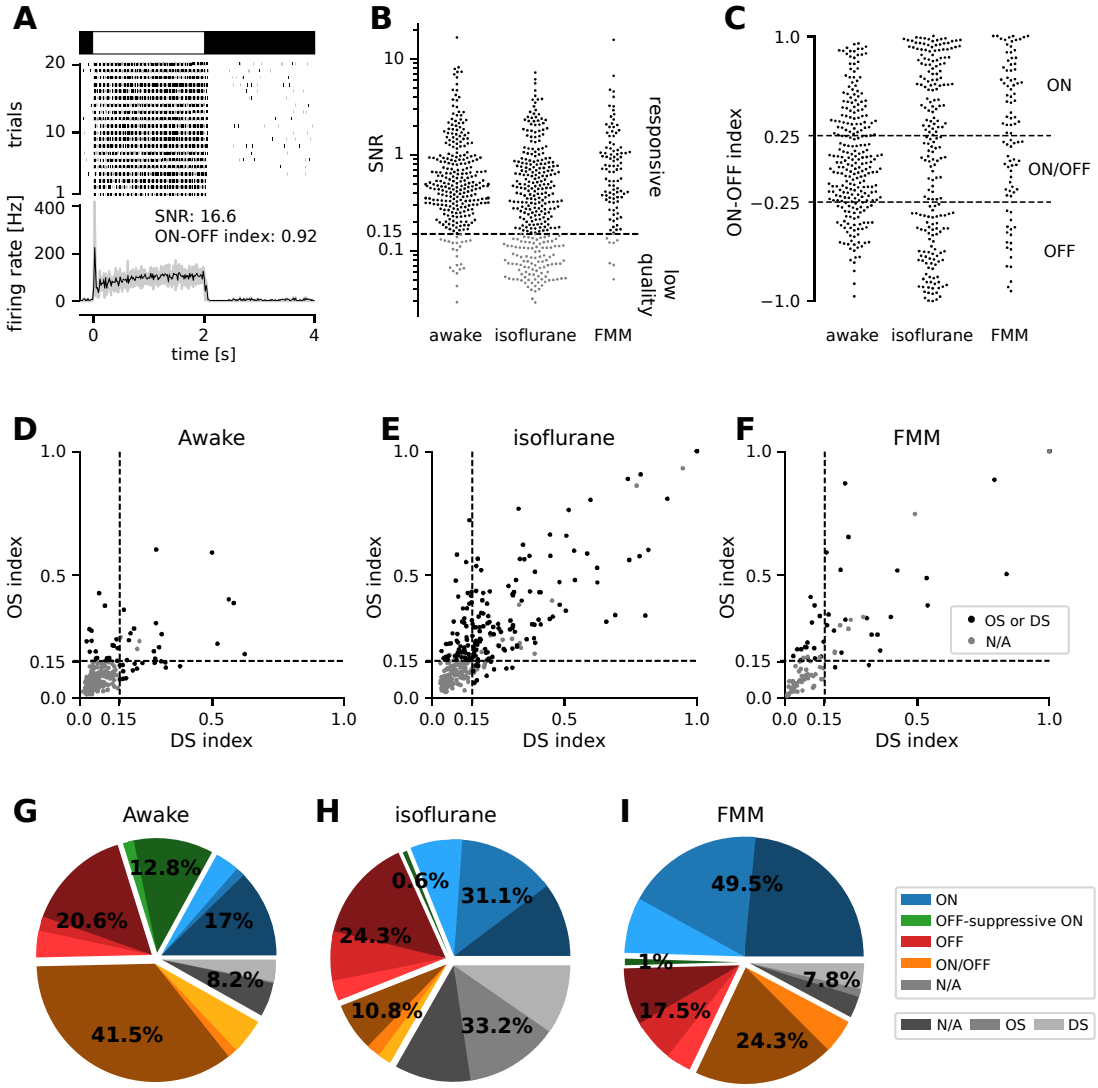

Figure 2: Physiological classification of retinal output responses *in vivo*. *A*: Representative retinal output responses to full-field contrast inverting stimuli: top, stimulus; middle, raster graph over trials; bottom, peri-stimulus time histogram (black, mean; gray, variance; signal-to-noise ratio (SNR), Eq.(1) in Methods; ON-OFF index, Eq.(2)). *B*: SNR of the retinal output responses in different recording conditions. We set a threshold at 0.15 to identify reliably responsive cells (black) and low-quality unclassifiable cells (gray). *C*: ON-OFF index distributions from the reliably responsive cells. While no apparent clusters were identified, we set a threshold at ±0.25 to categorize the response polarity into ON, ON/OFF, and OFF cells. Within the ON cells, we further identified those with an "OFF-suppressive" response to the full-field flickering stimulus (Figure 3). *D-F*: Distribution of DS/OS indices (Eq.(3)) in each recording condition (D, awake; E, isoflurane; F, FMM). We set a threshold at 0.15 (with $p<0.2$) to identify whether cells are OS/DS (black) or not (gray). *G-I*: Fraction of identified response classes *in vivo*: ON (blue; OFF-suppressive in green), OFF (red), ON/OFF (orange), and the rest unclassifiable cells ("N/A", gray). Cells in each category were further divided based on the OS/DS properties (hued). The OFF-suppressive ON cells were prominent in the awake condition (G, 36/282 cells), but rarely observed under anesthesia (H, isoflurane, 2/325 cells; I, FMM, 1/103 cells).

145 A distinguishing feature of awake recordings is an ongoing behavior of the animal
146 during recordings (Supplementary Figure 1). Behavioral states affect sensory processing (Neil
147 and Stryker, 2010), even at the early stages including the retina (Schröder et al., 2020). This
148 drove us to examine the effects of eye movements, pupil dynamics, as well as locomotion on
149 the retinal output *in vivo*.

150 First, we found that eye movements were not uniformly distributed in all directions
151 (Supplementary Figure 1H). Specifically, saccades were primarily in the horizontal directions
152 and much less in the vertical directions. Nevertheless, as reported previously (Samonds et al.,
153 2018; Miura and Scanziani, 2022), head-fixed awake mice did not frequently make eye
154 movements (0.06 ± 0.03 Hz; mean ± standard deviation, 19 animals) and thus their effects on
155 RGC activity were considered to be negligible in this study. The effects of microsaccades were
156 also negligible here as we mainly used full-field stimulation.

157 We next examined the relationship between pupil size and the retinal output dynamics.
158 They were both dependent on the light intensity level as evident by the pupillary reflexes
159 (Hatter et al., 2003) and the visual response polarities (Figure 2C), respectively. To analyze
160 their relationship, we thus focused on the recording period where the light intensity was
161 relatively stable over time (see Methods), and found that pupil size was correlated with RGC
162 firing in a response-polarity-dependent manner (Supplementary Figure 2A,B; Pearson's
163 R=0.38, p<0.001), likely mediated by the amount of light passing through the pupil.

164 Lastly, as reported previously (Schröder et al., 2020), we found that the activity of some
165 cells was significantly correlated with an animal's locomotion speed (Supplementary Figure
166 3C,D). While there was a positive correlation between pupil size and locomotion speed (0.34
167 ± 0.20 from 19 animals; see also Erisken et al., 2014), unlike the pupil size effects, the
168 locomotion effects on the retinal output *in vivo* was not dependent on the visual response
169 polarity of the cells (Supplementary Figure 3D; Pearson's R=0.11, p=0.3). Thus, the
170 correlation between locomotion and RGC firing dynamics cannot be simply explained by the
171 light intensity fluctuation due to the associated pupil size dynamics.

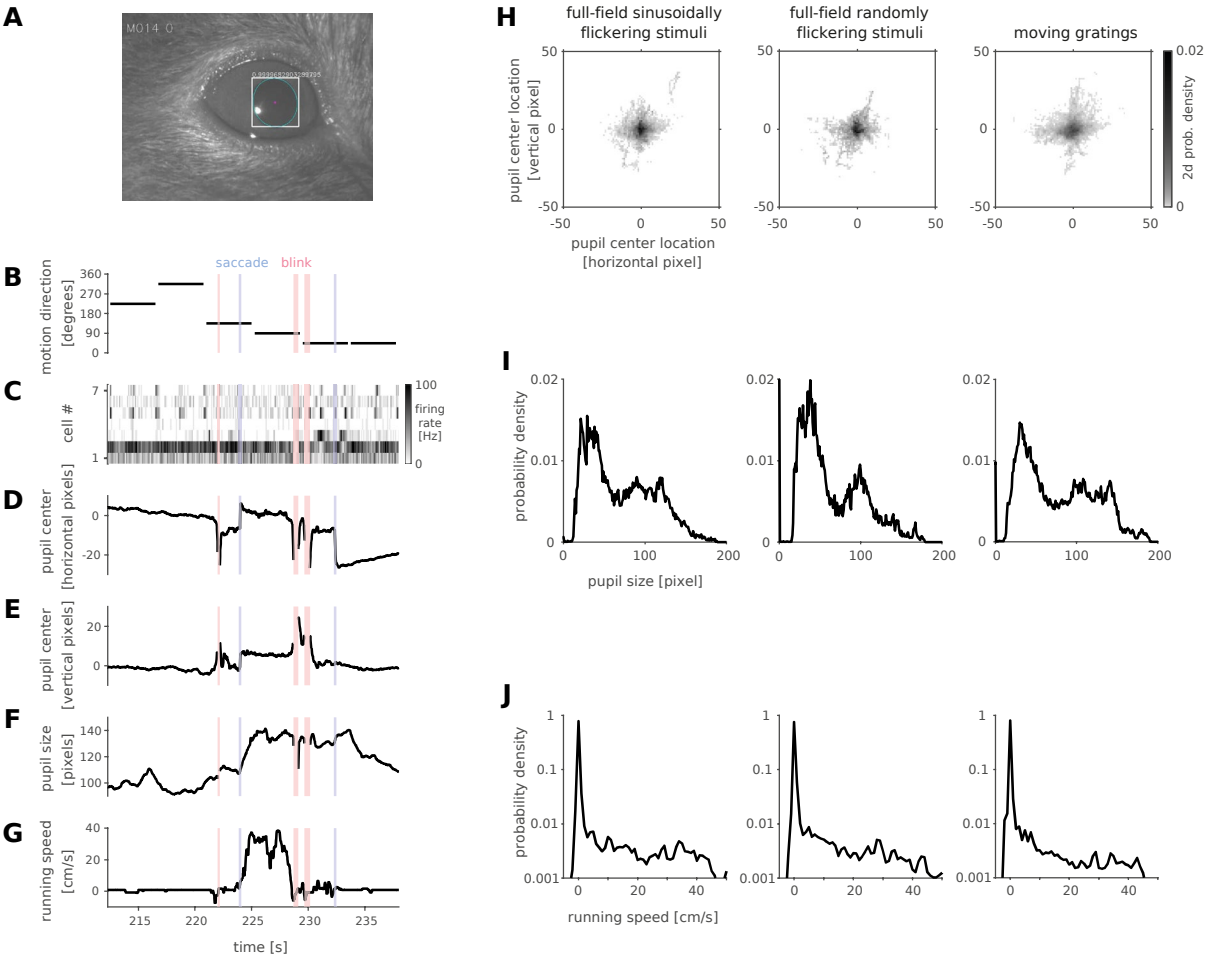

Supplementary Figure 1: Eye motion and behavioral data analysis. *A*: Example eye-tracking frame of an awake mouse eye. Cyan ellipse shows the pupil edge, while magenta dot shows its center location. *B-G*: Representative dynamics of simultaneously recorded data in an awake head-fixed condition (B, the presence and direction of the moving gratings stimulus; C, firing rate heat map of simultaneously recorded seven RGCs; D and E, horizontal and vertical coordinates of the pupil center location in each frame, respectively; F, pupil size defined as a mean of the major and minor axis of the ellipse fitted to the pupil edge in each frame; and G, running speed of the mouse). Red shades indicate eye blinks, whereas the blue vertical lines indicate saccades. Note that blinks and saccades occurred only once in a while (0.06 ± 0.03 Hz; mean ± standard deviation, 19 animals); and that the pupil size (F) is positively correlated with the running speed (G) in general (0.34 ± 0.20; 19 animals). *H-J*: Probability density of pupil center location (H), pupil size (I), and running speed (J) across different visual stimulation periods (from left to right, full-field sinusoidally flickering stimuli; randomly flickering full-field stimuli; and moving gratings; 19 animals).

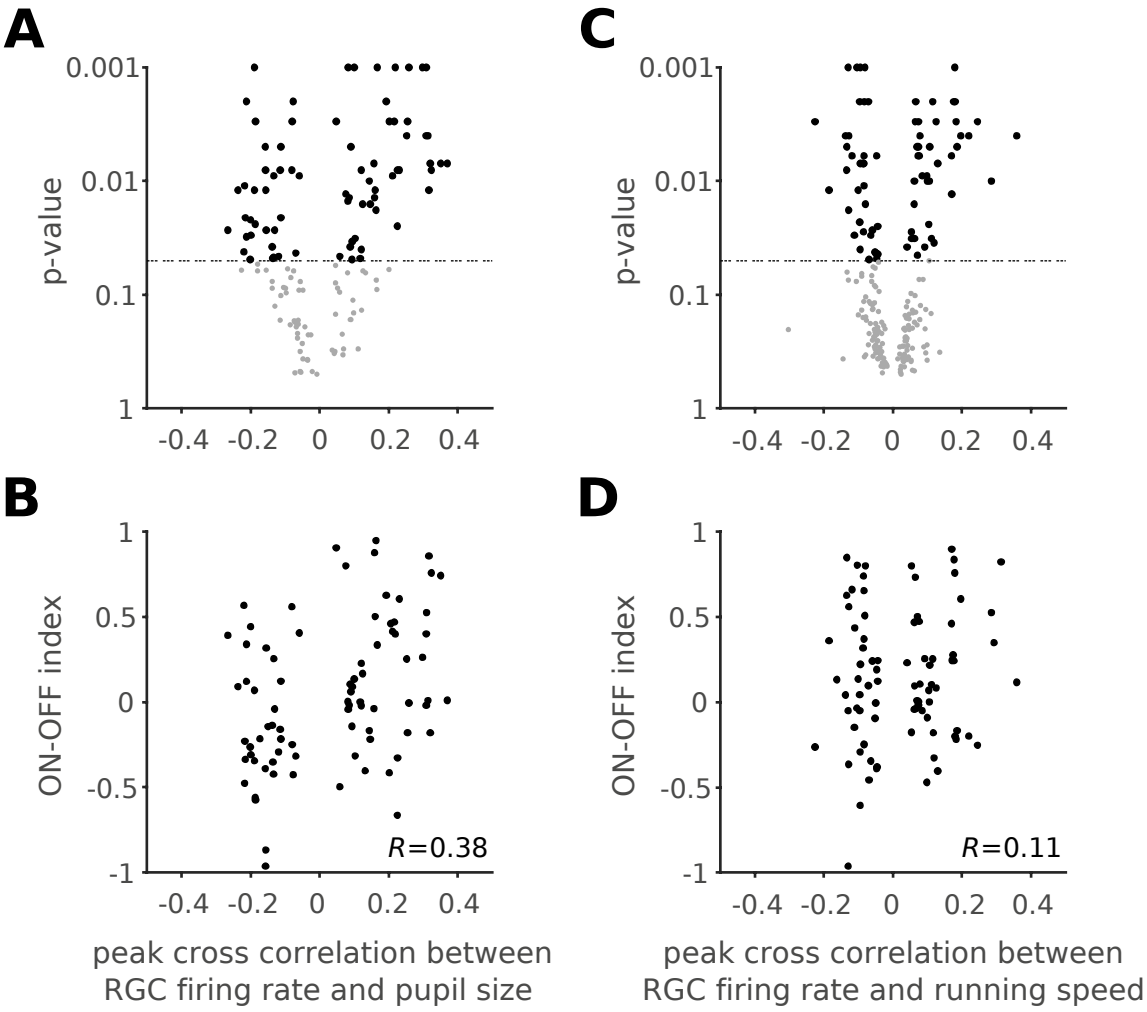

Supplementary Figure 2: Retinal output was correlated with an animal's behavioral states. *A,B*: Peak cross-correlation values between retinal output and the animal's pupil size, plotted against the *p*-values calculated by a shuffling analysis (1,000 repetitions, see Methods; A) or the ON-OFF index (B): black, correlation with $p<0.05$; gray, correlation with $p>0.05$. The pupil size effects on RGC firing were significantly correlated with the ON-OFF index (B; Pearson's $R=0.38$, $p<0.001$). *C,D*: Corresponding plots for the peak cross-correlation values between retinal output and the animal's running speed. The locomotion effects on RGC firing were not significantly correlated with the ON-OFF index (D; Pearson's $R=0.11$, $p=0.3$).

Higher firing in awake than in anesthetized mice

For characterizing the retinal output properties *in vivo*, we first analyzed the responses to full-field sinusoidally flickering stimuli that linearly changed the amplitude over time (from 0 to 100% contrast for 10 s; see Figure 3A-C for representative responses). We fitted to the response an even-power of sine function, weighted with a sigmoid envelope (Eq.(6) in Methods), and examined the curve-fit parameter values to analyze the response properties in different recording conditions.

First, we found significantly higher baseline firing rates in awake mice ($B = 20 \pm 27$ Hz; median ± interquartile range) than in those under anesthesia (isoflurane, 2 ± 6 Hz, $p < 0.001$, *U*-test; FMM, 2 ± 4 Hz, $p < 0.001$; Figure 3D). Awake ON cells had particularly high baseline activity (up to ~100 Hz) and showed a prominent reduction in firing rates in response to light decrements (see Figure 3B for example). In contrast, due to this high baseline activity, many of them showed virtually no responses to light increments ($N = 36$ out of 84), except for a sharp rebound response to a full-contrast inversion ($N = 26$ out of 36; see Figures 2A and 3B for example). These ON cells had negative amplitudes in the curve fit (Figure 3E, green) with the same response phase as OFF cells (Figure 3F; see Figure 3A for a representative OFF cell's responses). This indicates that they primarily encode light decrements by decreasing firing from their high baseline firing rates (62 ± 32 Hz, mean ± standard deviation), rather than light increments by increasing firing as conventional ON cells do (Masland, 2012; Sanes and Masland, 2015; Baden et al., 2016; Jouty et al., 2018). We thus categorized these cells independently as an "OFF-suppressive" class (Figure 2G). This is likely an emerging property of the cells due to high baseline firing in awake mice. Indeed, such responses were barely observed in anesthetized animals (isoflurane, 2/325 cells; FMM, 1/103 cells; Figure 2H,I) where the baseline firing rate was generally low (Figure 3D). As expected from previous *ex vivo* studies (Masland, 2012; Sanes and Masland, 2015; Baden et al., 2016; Jouty et al., 2018), anesthetized ON cells increased firing upon light increments (see Figure 3C for a representative response). Positive amplitudes in the curve fit (Figure 3E) with an opposite

response phase from OFF cells (Figure 3F) further support that these ON cells encode light increments. These data suggest that the retinal coding depends on the baseline firing level of RGCs.

Second, we found that the awake responses had a larger dynamic range than those under anesthesia. Specifically, the absolute amplitude of the evoked responses from the baseline was larger for the awake condition (Figure 3E; awake, $|A| = 45 \pm 55$ Hz, median ± interquartile range; isoflurane, 30 ± 31 Hz, *p*<0.001, Mann-Whitney *U*-test against awake data; FMM, 27 ± 33 Hz; *p*<0.001). Moreover, the sigmoid envelope had a higher midpoint (awake, $t_0 = 70 \pm 61$ % contrast; isoflurane, 45 ± 32 % contrast, *p*<0.001; FMM, 45 ± 44 % contrast, *p*<0.001) and a lower steepness (awake, $\lambda = 0.44 \pm 0.53$ /s; isoflurane, 0.67 ± 0.79 /s, *p*<0.001; FMM, 0.69 ± 0.62 /s, *p*<0.001) for the awake responses than for the anesthetized ones.

We next examined the sensitivity to contrast. At low stimulus contrast, we found a higher sensitivity in the awake condition (estimated evoked response at 10% contrast = 7 ± 13 Hz, median ± interquartile range) than under anesthesia (isoflurane, 4 ± 12 Hz, *p*<0.001, Mann-Whitney *U*-test; FMM, 3 ± 10 Hz, *p*<0.001). However, the maximum sensitivity to a change in contrast – i.e., the slope size at the midpoint of the sigmoid – was comparable between the awake and anesthetized conditions ($|A\lambda/4| = 5 \pm 11$ Hz / %contrast; isoflurane, 6 ± 9 Hz / %contrast; FMM, 5 ± 7 Hz / %contrast; p = 0.1, Kruskal-Wallis test).

We also found a significant phase shift in the responses between the recording conditions (Figure 3F). This phase parameter in the curve fit represents the position of the response peak relative to the sinusoidal stimulus intensity patterns (see Methods for details), and we identified two clusters in each data set: the one with negative phase for ON cells (Figure 3F, blue) and the other with positive phase for OFF and OFF-suppressive ON cells (Figure 3F, red and green, respectively). ON/OFF cells were found in either cluster, depending on the relative strength of their responses to light increments versus light decrements (Figure 3F, orange). In both clusters, we found that the phase was on average smallest for the awake

condition (-1.9 ± 0.6 and 1.7 ± 0.6 radian, respectively; mean ± standard deviation; isoflurane, -0.9 ± 0.6 and 2.0 ± 0.5 radian; $p < 0.001$ for both cases, *t*-test), while largest for the FMM anesthesia (-0.5 ± 0.8 and 2.3 ± 0.5 radian; *p*=0.007 and *p*=0.044 against corresponding isoflurane data, respectively). This implies that the response dynamics are faster in awake mice than those under anesthesia, especially with FMM.

Finally, we analyzed the retinal output properties between different visual response polarities by combining data across recording conditions (ON, 199 cells in total; OFF, 121 cells; and ON/OFF, 170 cells). We found that the baseline firing rate was higher for ON/OFF cells (17 ± 24 Hz; median ± interquartile range) than for ON or OFF cells (5 ± 24 and 6 ± 10 Hz, respectively; *p*<0.001, Kruskal-Wallis test). Otherwise we did not find any statistically significant dependency on the response polarity at the population level.

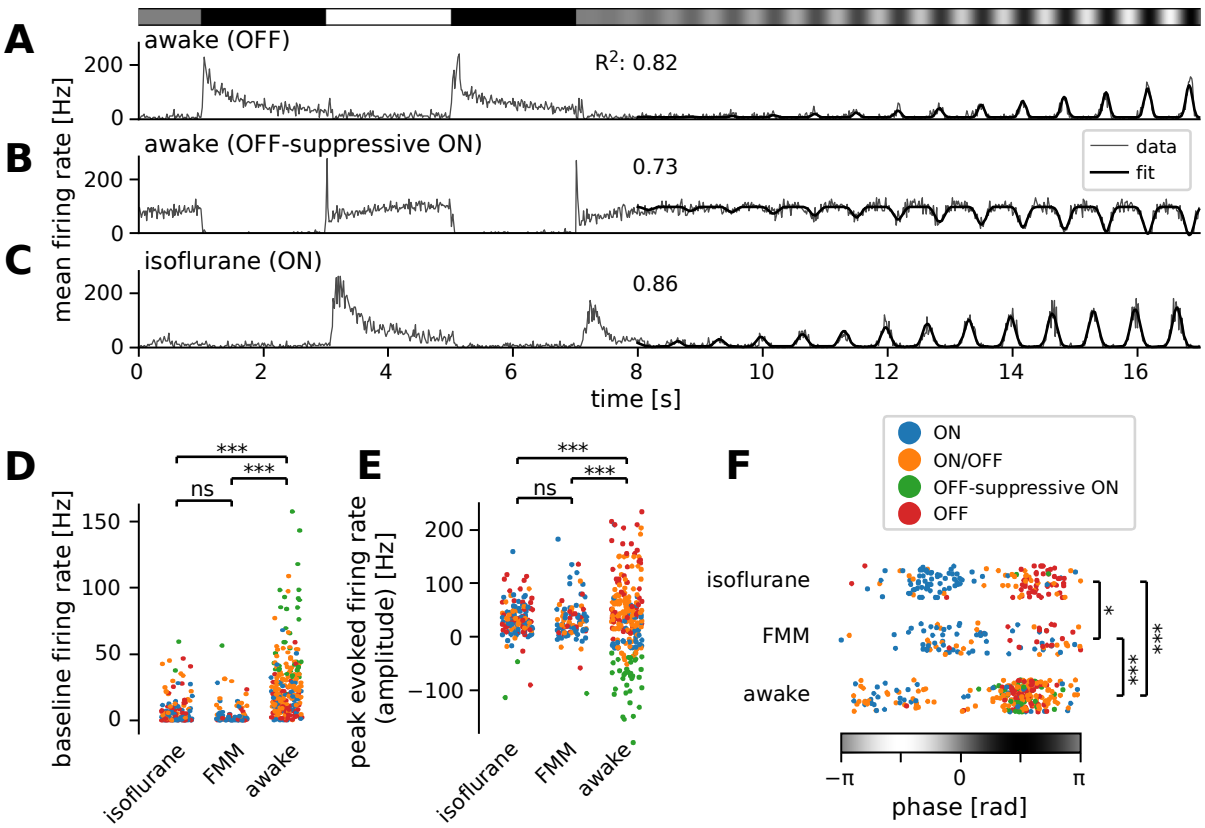

Figure 3: Many ON retinal ganglion cells showed suppressive OFF responses in awake condition. *A-C*: Mean firing rate of representative cells in response to a sinusoidally-flickering stimulus with increasing contrast in the awake (A, OFF; B, OFF-suppressive ON, the same cell as in Figure 2A) or anesthetized conditions (C, ON). Overlaid with the peri-stimulus time histogram (gray) is the model fit (black, Eq.(6) in Methods). The number on top indicates the fit quality (explained variance R^2 in Eq.(5)). *D-F*: population data of the model parameters (D, baseline B; E, amplitude A; F, phase ϕ) across different conditions: isoflurane anesthesia ($N = 147$), FMM anesthesia ($N = 95$) and awake ($N = 247$ in total). The sinusoidal stimulus pattern relative to the response peak is also indicated at the bottom of F. Cell types are color-coded as in Figure 2 (blue, ON; green, OFF-suppressive ON; red, OFF; orange, ON/OFF). Note high baseline with negative amplitude and positive phase for the OFF-suppressive ON cells, which were predominantly found in the awake condition: ***, $p < 0.001$; **, $p < 0.01$; *, $p < 0.05$; ns, non-significant (D, *U*-test; E, *U*-test on the absolute values; F, *t*-test).

Faster response kinetics in awake than in anesthetized mice

To better characterize the kinetics of retinal output *in vivo*, we next analyzed the responses to full-field sinusoidal flickers at different temporal frequencies (Figure 4). In awake mice, most cells responded faithfully to all the stimulation frequencies we tested from 1.875 to 15 Hz (see Figure 4A for example). Some awake cells showed the largest responses to the 15 Hz stimulation (Figure 4A; curve fit quality with Eq. (4)), suggesting that they were possibly tuned to even higher frequencies. In the anesthetized conditions, in contrast, retinal output responses typically followed the stimulation frequencies up to 7.5 Hz, but failed to do so at 15 Hz (see Figure 4B for example). For quantification, we fitted an even-power of sine function to the responses (Eq.(4) in Methods) and set a threshold of the curve fit quality (defined as the explained variance; Eq.(5)) at 0.2 to select cells with robust responses (Figure 4C,D). In the awake condition, a larger number of cells responded well at medium frequencies (3.75 Hz, 63%; 7.5Hz, 71%) than at a low frequency (1.875 Hz, 59%); and the majority of the awake cells remained responsive to a high frequency stimulus (15 Hz, 47%). Under anesthesia, in contrast, the fraction of responsive cells was the largest at a low frequency (1.875 Hz; isoflurane, 77%; FMM, 67%). Fewer cells responded robustly at faster flicker rates (3.75 Hz and 7.5 Hz; isoflurane, 69% and 67%, respectively; FMM, 63% and 59%), and only a small fraction of the anesthetized cells were able to follow the stimulation frequency at 15 Hz (isoflurane, 13%; FMM, 3%). Consistent with the analysis of the response phase (Figure 3), these outcomes indicate that the retinal output dynamics are faster in awake animals than those under anesthesia, especially for FMM.

Across the response polarities, we found that ON/OFF cells (N=170 in total) were most responsive at a medium frequency (7.5Hz, 59%), while ON or OFF cells (N=199 and 121, respectively) were generally responsive from low to medium frequencies (1.875-7.5 Hz; 68-73% and 79-82%, respectively). Indeed, the fraction of responsive cells under our criteria was significantly lower for ON/OFF cells (1.875 Hz, 46%; 3.75 Hz, 49%) than for ON or OFF cells at low frequencies ($p<0.001$ for both frequencies, two-proportion z-test). No dependency on

the response polarity was found for a high frequency stimulation (15 Hz; ON, 25%; OFF, 29%; ON/OFF, 31%).

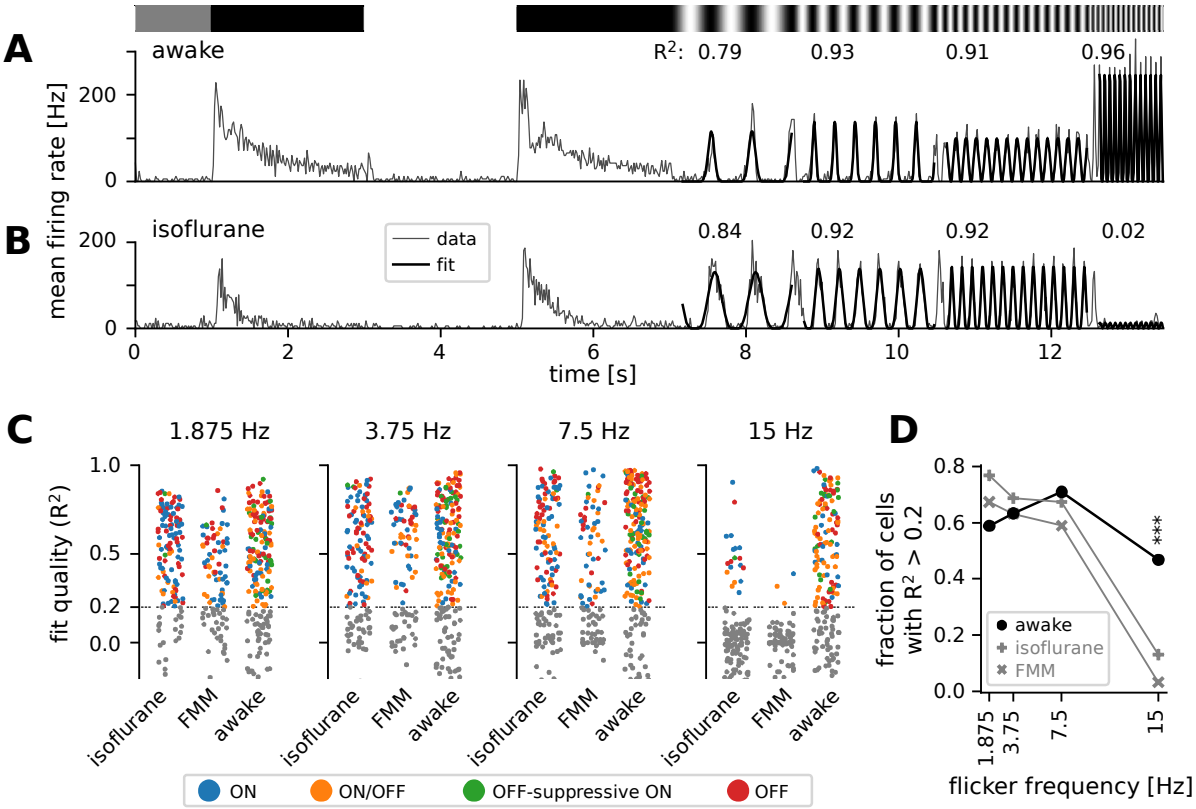

Figure 4: Retinal output showed higher temporal frequency sensitivity in awake than in anesthetized mice. *A*: Representative retinal output (gray, mean firing rate over 10 trials) in an awake condition in response to full-field sinusoidally flickering stimuli at different temporal frequencies (1.875, 3.75, 7.5 and 15 Hz), following full-field contrast inversions. Overlaid is the curve fit (Eq.(4) in Methods; black). The number on top is the explained variance of the curve fit (R^2, Eq. (5) in Methods), representing the fit quality. *B*: Representative retinal output responses under isoflurane anesthesia (shown in the same format as in A). *C*: Population data of the fit quality at four different stimulus frequencies in the awake ($N = 248$) or anesthetized conditions (isoflurane, $N = 147$; FMM, $N = 95$), color-coded for the responses class as in Figure 2. The fit quality threshold was set to be 0.2 (black, $R^2 \geq 0.2$; gray, $R^2 < 0.2$). *D*: Fraction of the cells with the fit quality above the threshold across different conditions (awake, black line with circles; isoflurane, gray line with vertical crosses; FMM, gray line with diagonal crosses), representing the frequency tuning of the retinal output at the population level. A significantly larger fraction of cells was responsive at 15 Hz in the awake condition than in the anesthetized conditions (***, $p < 0.001$ for both isoflurane and FMM; two-proportion *z*-test).

320 # Comparison of retinal output properties between *in vivo*
321 # and *ex vivo*

322 We have thus far focused on the retinal output properties *in vivo*, and showed higher baseline
323 firing rates (Figure 3) and faster response kinetics (Figure 4) in awake mice than in those
324 under anesthesia. We next asked if RGC responses differ between *in vivo* and *ex vivo*
325 conditions. This is a critical comparison because retinal physiology has been mostly studied
326 and best characterized in an isolated preparation (Gollisch and Meister, 2010; Sanes and
327 Masland, 2015), but little is known about it in awake animals (Weyand, 2007; Liang et al., 2018,
328 2020; Schröder et al., 2020; Sibille et al., 2022). To what extent can we translate our
329 knowledge on the retina from *ex vivo* to *in vivo*? Here we exploited stimulus ensemble
330 statistical techniques ("reverse correlation"; Meister et al., 1994; Chichilnisky, 2001) to
331 systematically characterize the visual response properties and make a direct comparison
332 across different recording conditions in the linear-nonlinear cascade model framework (see
333 Methods for details). Specifically, using full-field white-noise stimuli, we analyzed 1) the linear
334 temporal filter (Figure 5), estimated by the spike-triggered average (STA) stimulus, i.e., the
335 mean stimulus that triggered spiking responses; and 2) the static nonlinear gain function
336 (Figure 6), i.e., an instantaneous mapping of the STA output to the neural responses (Eq. (7)
337 in Methods). Here we reanalyzed the existing data sets for *ex vivo* recordings (696 cells from
338 18 isolated mouse retinas recorded at 37 °C; Vlasiuk and Asari, 2021).

339 ## Faster response kinetics in awake condition than *ex vivo*

340 We identified a good quality STA in more than two-thirds of the cells recorded *in vivo* (e.g.,
341 Figure 5A). To compare the temporal dynamics of the STAs across different recording
342 conditions, we used the following two measures: 1) the first peak latency of the STA estimated
343 from a difference-of-Gaussian curve fit (Figure 5A); and 2) spectral peak frequency calculated
344 by the Fourier transform of the fitted curve (Figure 5B). Consistent with the results measured
345 by the flickering stimuli at different frequencies (Figure 4), we found faster kinetics in awake

346 animals than in anesthetized ones (Figure 5C,D): i.e., significantly shorter peak latencies
347 (awake, 47 ± 18 ms, mean ± standard deviation; isoflurane, 77 ± 19 ms, $p < 0.001$, *t*-test;
348 FMM, 87 ± 24 ms, $p < 0.001$; Figure 5C) and higher peak frequencies (awake, 8.5 ± 2.9 Hz;
349 isoflurane, 4.6 ± 1.6 Hz, $p < 0.001$; FMM, 3.7 ± 1.2 Hz, $p < 0.001$; Figure 5D). Interestingly,
350 we identified that the *ex vivo* data lied in-between. The *ex vivo* STAs had significantly longer
351 peak latencies (64 ± 28 ms, $p < 0.001$) and lower peak frequencies (4.3 ± 1.8 Hz, $p < 0.001$)
352 than the awake ones. In contrast, the peak latencies were significantly shorter in an isolated
353 retinal preparation than in the anesthetized conditions (isoflurane, $p < 0.001$; FMM, $p < 0.001$),
354 while the peak frequencies were comparable between these conditions (isoflurane, $p = 0.3$;
355 FMM, $p = 0.052$).

356 We further analyzed the STA dynamics across different cell classes. For clustering the
357 STAs obtained in each recording condition, we used the principal component analysis (PCA;
358 see Methods for details). As in previous *ex vivo* studies (Gollisch and Meister, 2008; Asari and
359 Meister, 2014), the first two principal components accounted for most of the variance (78-86%,
360 collectively), and the four quadrants of the PCA biplot generally represented distinct filter
361 shapes, corresponding to monophasic OFF (mono-OFF), biphasic OFF (bi-OFF), monophasic
362 ON (mono-ON), and biphasic ON (bi-ON) response classes, respectively. In all recording
363 conditions, no apparent cluster was found in this feature space, leading to a continuum of the
364 STA shape patterns across populations (Figure 5E-H). Nevertheless, we identified two
365 features that were different between *ex vivo* and *in vivo*, especially distinct in the awake
366 condition. First, while the monophasic cells were generally slower than the biphasic ones,
367 differences in the peak latencies were much larger in the *ex vivo* (Figure 5G; mono-ON $83 \pm$
368 24 ms versus bi-ON 58 ± 31 ms, $p < 0.001$, *t*-test; mono-OFF 67 ± 29 ms versus bi-OFF $48 \pm$
369 8 ms, $p < 0.001$) or anesthetized conditions (Figure 5E, isoflurane: mono-ON 91 ± 22 ms, bi-
370 ON 67 ± 6 ms, $p < 0.001$; mono-OFF 89 ± 14 ms, bi-OFF 68 ± 8 ms, $p < 0.001$; Figure 5F,
371 FMM: mono-ON 97 ± 30 ms, bi-ON 78 ± 11 ms, $p = 0.051$; mono-OFF 103 ± 13 ms, bi-OFF
372 70 ± 11 ms, $p < 0.001$) than in the awake condition (Figure 5H; mono-ON 51 ± 20 ms, bi-ON

44 ± 19 ms, $p = 0.6$; mon-OFF 51 ± 19 ms, bi-OFF 43 ± 12 ms, $p = 0.1$). Second, we found that ON cells were significantly slower than OFF cells *ex vivo* (mono-ON versus mono-OFF, $p = 0.002$; bi-ON versus bi-OFF, $p = 0.03$), but not *in vivo* ($p > 0.2$ in all the conditions examined). Taken together, our results suggest that awake responses are faster and their kinetics are more similar across different cel classes than *ex vivo* or anesthetized responses.

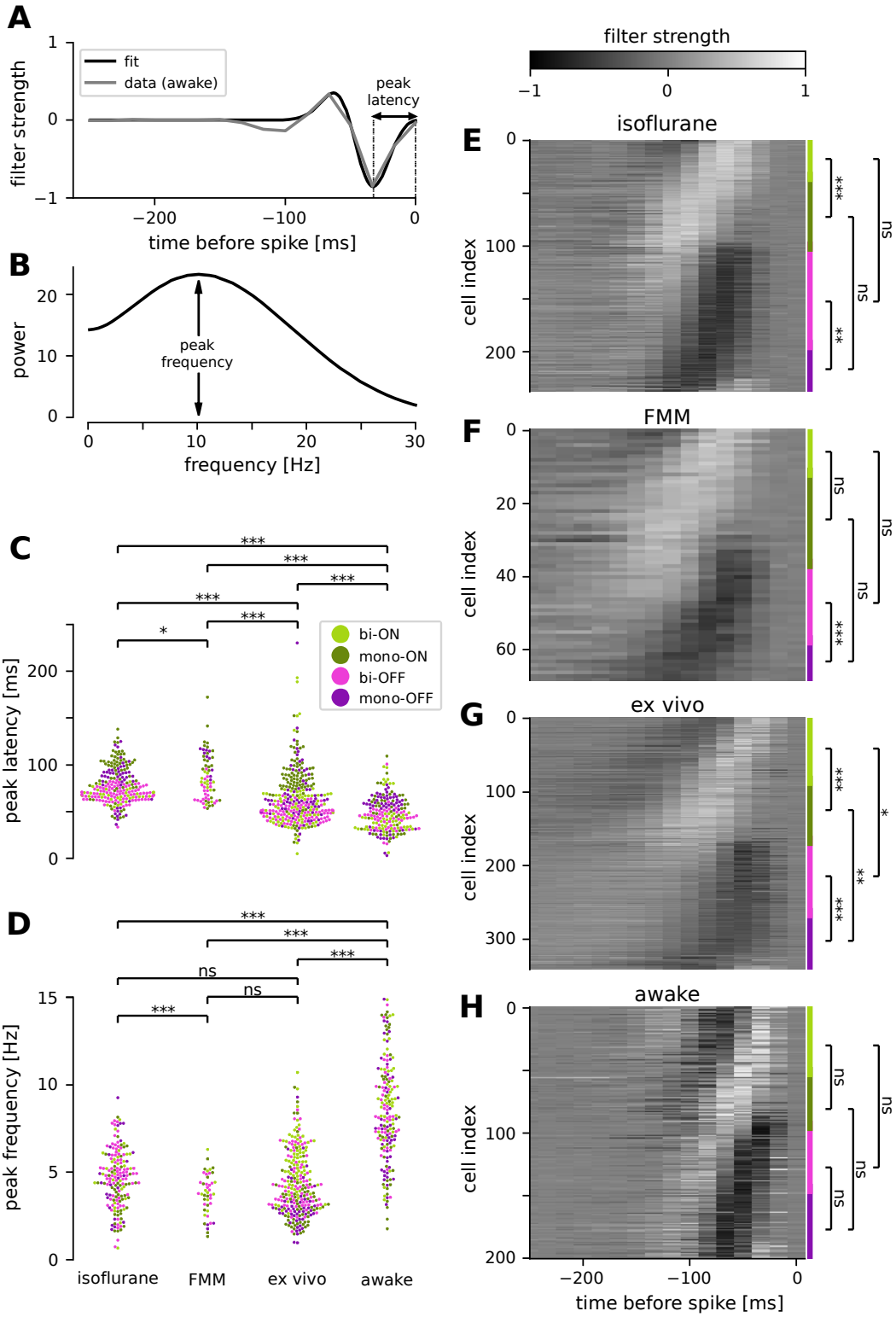

Figure 5: Retinal ganglion cells showed faster response dynamics in awake condition than in anesthetized or *ex vivo* conditions. *A*: Temporal filter of a representative awake cell (gray, spike-triggered average (STA) of the full-field randomly flickering stimulus) and a difference-of-Gaussian curve fit (black) for estimating the latency of the first peak. *B*: Power spectra of the example filter in A, based on the curve fit, for estimating the peak frequency. *C,D*: Population data of the peak latencies (C) and frequencies (D) across different conditions (light green, biphasic ON; dark green, monophasic ON; pink, biphasic OFF; violet, monophasic OFF). Here and thereafter, ***, $p < 0.001$; **, $p < 0.01$; *, $p < 0.05$; ns, non-significant (*t*-test). The filter types were identified by the quadrants of the PCA biplot (see Methods for details). *E-H*: Population data of the temporal filters across different conditions: from top to bottom, isoflurane anesthesia (E, $N = 238$), FMM anesthesia (F, $N = 69$), *ex vivo* (G, $N = 342$) and awake (H, $N = 201$). The four filter types are indicated on the right with corresponding colors.

Higher spiking activity in awake condition than *ex vivo*

How does a recording condition affect the firing properties of RGCs? The mean firing rate during the white-noise stimulus presentation was significantly higher in awake (34.9 ± 24.6 Hz; mean ± standard deviation) than in all the other recording conditions (isoflurane, 13.0 ± 13.1 Hz; FMM, 10.9 ± 10.7 Hz; *ex vivo*, 6.9 ± 6.6 Hz; all with $p < 0.001$, *t*-test in the logarithmic scale; Figure 6A). Importantly, this is presumably not due to differences in the stimulus condition. The maximum projected light intensity was comparable between *in vivo* (~31 $\mathrm{mW/m^2}$ at the eye; see Methods) and *ex vivo* setups (~36 $\mathrm{mW/m^2}$ on the isolated retina; Vlasiuk and Asari, 2021). Due to absorption by the eye optics, however, photon flux at the retina was estimated to be ~10 times lower for *in vivo* than for *ex vivo* recordings (on the order of 10^3 and 10^4 R*/photoreceptor/s, respectively; see Methods). Furthermore, awake mice show pupillary reflexes (Supplementary Figure 1), leading to a smaller amount of light impinging on the retina than under anesthesia. Nevertheless, these differences in the lighting conditions cannot explain the higher firing and faster kinetics in the awake cells (Figure 6A and Figure 5) because RGCs typically show larger and faster responses to brighter and higher-contrast stimuli (Baccus and Meister, 2002; Wang et al., 2011).

For a further analysis, we examined the static nonlinear gain function of the recorded cells (Eq. (7) in Methods). This gain function accounts for nonlinearity associated with spike generation, such as spike threshold and firing rate saturation, and is generally well explained by a sigmoid function (see Figure 6B for example). For quantification, we assessed the neutral firing rate of the cells where the input to the gain function is zero, i.e., the firing rate in the presence of "neutral" stimuli that are orthogonal to the cell's STA. Consistent with the results on the baseline firing rates measured by the sinusoidally flickering stimuli (Figure 3), the neutral firing rate was significantly higher in the awake condition (29.3 ± 22.5 Hz, mean ± standard deviation) than those under anesthesia (isoflurane, 9.5 ± 11.9 Hz, $p < 0.001$, *t*-test on a log scale; FMM, 7.5 ± 9.3 Hz, $p < 0.001$; Figure 6C). We also found that the neutral firing rates *ex vivo* (5.5 ± 7.1 Hz) were as low as those in the anesthetized conditions (isoflurane, $p = 0.02$; FMM, $p = 0.1$), and significantly lower than those in the awake condition ($p < 0.001$).

We further identified two distinct features in the gain function properties between *ex vivo* and *in vivo* responses. First, ON cells generally had a higher gain than OFF cells *ex vivo* (Figure 6F), whereas such cell-type specific differences were not observed *in vivo* (isoflurane, Figure 6D; FMM, Figure 6E; awake, Figure 6G). Second, the midpoint of the sigmoid fitted to *ex vivo* responses (1.6 ± 1.4, median ± interquartile range) was significantly higher than that for *in vivo* responses (isoflurane, 1.1 ± 0.9; FMM, 1.1 ± 0.8; awake, 0.8 ± 1.0; all with $p < 0.001$, Mann-Whitney *U*-test; Figure 6H). In agreement with the outcomes obtained with the sinusoidally flickering stimulus (Figure 3), this suggests that *in vivo* responses are more linearized to cover a larger dynamic range, especially in the awake condition due to high neutral responses (Figure 6G). Indeed, while certain batch effects existed across recording sessions (Supplementary Figure 3), the dynamic range computed from the gain function (see Methods) was generally largest in the awake condition (56 ± 54 Hz; median ± interquartile range) and significantly larger for *in vivo* (isoflurane, 26 ± 30 Hz; FMM, 29 ± 27 Hz) than for *ex vivo* (12 ± 12 Hz, all with $p < 0.001$, Mann–Whitney *U*-test).

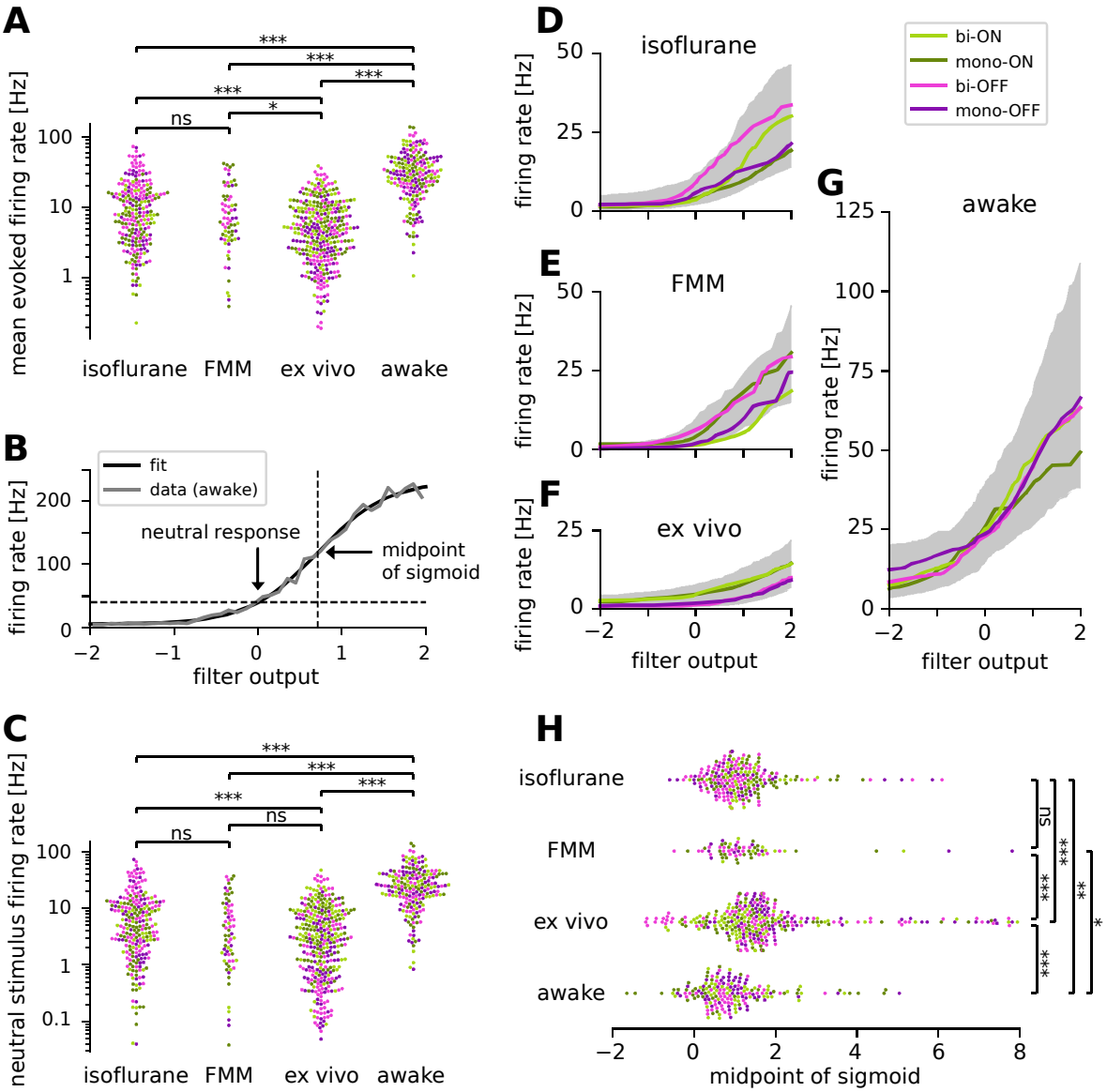

Figure 6: Retinal ganglion cells showed higher firing activity in awake condition than in anesthetized or *ex vivo* conditions. Cell classes are color-coded as in Figure 5 (light green, biphasic ON; dark green, monophasic ON; pink, biphasic OFF; violet, monophasic OFF). *A*: Population data of the mean firing rates during the stimulus presentation period in four different recording conditions (isoflurane, FMM, *ex vivo*, and awake): ***, $p < 0.001$; **, $p < 0.01$; *, $p < 0.05$; ns, non-significant (*t*-test on the logarithm of firing rates). *B*: Static nonlinear gain function of a representative awake cell (the same one as in Figure 5A), estimated by the stimulus ensemble statistical techniques applied to the responses to a full-field randomly flickering stimulus (gray, Eq.(7) in Methods; black, sigmoid curve fit with the midpoint at 0.71). Note a high neutral stimulus response (40 Hz) defined as the firing rate at zero filter output (i.e., in the presence of stimuli orthogonal to the cell's STA). *C*: Population data of the neutral stimulus responses in each recording condition (in the same format as in A). *D-G*: Population data of the static nonlinear gain function (median for each cell type in corresponding colors; gray, interquartile range of all cells) across different conditions: isoflurane anesthesia (D, $N = 238$), FMM anesthesia (E, $N = 69$), *ex vivo* (F, $N = 342$), and awake condition (G, $N = 201$). *H*: Population data of the midpoint of the sigmoid nonlinearity in each recording condition: ***, p<0.001; Mann-Whitney *U*-test.

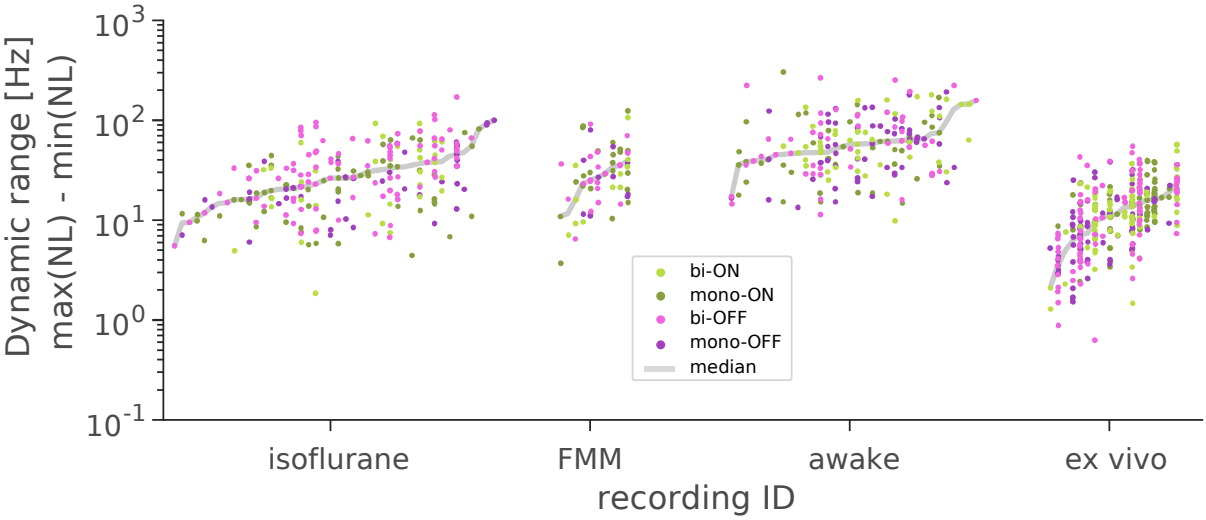

Supplementary Figure 3: Batch effects in the datasets. Dynamic range was computed for each cell as the difference between the maximum and minimum firing rates of the static nonlinear gain function (Figure 6D-G), and shown for each recording session in columns (dark green, monophasic ON; light green, biphasic ON; pink, biphasic OFF; violet, monophasic OFF; gray line, median). Some variabilities were present across preparations in each recording condition (isoflurane, *N*=44 recording sessions; FMM, *N*=10; awake, *N*=34; or *ex vivo*, *N*=18), but the batch effects were not large enough to eliminate any particular data set.

Retinal outputs in awake mice are less efficient but more linearly decodable

Our experimental data demonstrated that retinal outputs in awake mice had distinct characteristics compared to those under anesthesia or *ex vivo*, such as higher baseline firing rates (Figures 3 and 6), faster response kinetics (Figures 3-5), and a larger dynamic range (Figuress 3 and 6; Supplementary Figure 3). What are the implications on retinal coding? To address this question, we quantitatively analyzed our data in three ways.

First, we took an information theoretic approach and calculated the information conveyed by the retinal output spike trains recorded under different conditions (Figure 7; see Methods). Overall, we found that *in vivo* responses had a slightly but significantly higher information rate in bits per second (Figure 7A; isoflurane, 8.6 ± 5.9 bits/s; FMM, 7.6 ± 3.6 bits/s; awake, 7.5 ± 2.2 bits/s; median ± interquartile range) than *ex vivo* responses (6.2 ± 1.9 bits/s; $p<0.001$, $p=0.004$, $p<0.001$, respectively; Mann-Whitney *U*-test), but a lower information

rate in bits per spike (Figure 7B; isoflurane, 1.2 ± 1.6 bits/spike; FMM, 1.3 ± 1.4 bits/spike; and awake, 0.3 ± 0.3 bits/spike; against *ex vivo*, 2.3±1.9 bits/spike; all with p<0.001). In particular, the amount of information conveyed by a single spike in awake cells was the lowest due to high average firing rates (34 ± 25 Hz; mean ± standard deviation). This indicates that the retinal coding *in vivo* is less efficient than that *ex vivo* (Schwartz, 2021).

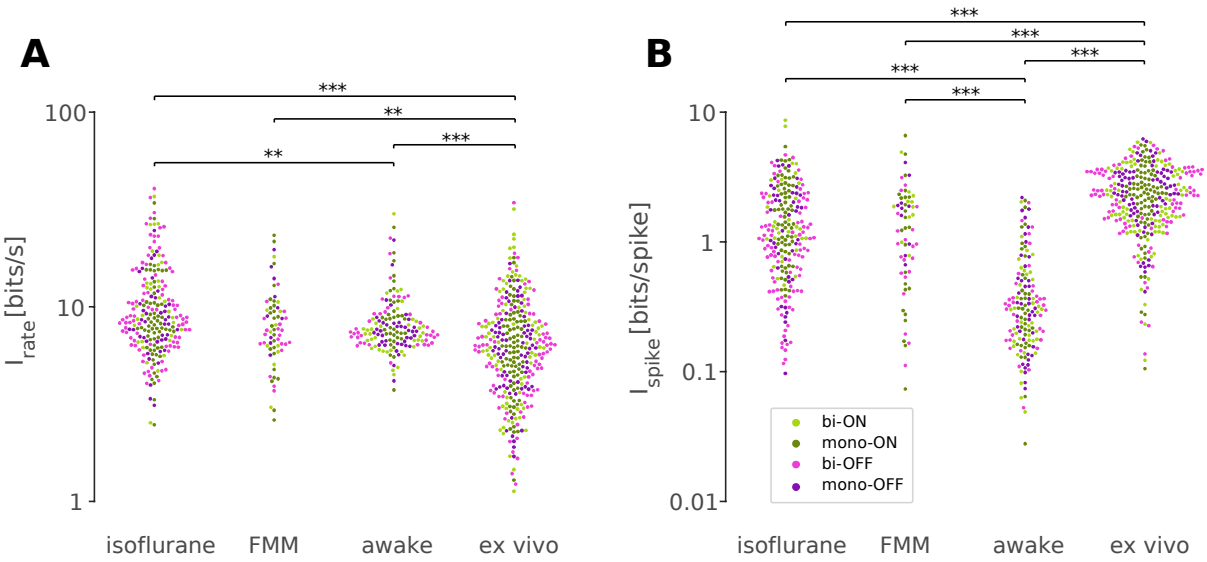

Figure 7: Retinal responses *in vivo* have a lower information rate in bits per spike but a higher rate in bits per second than those *ex vivo*. Information rate conveyed by retinal output spike trains in bits per second (A) and in bits per spike (B; Eq.(8) in Methods) in response to randomly flickering full-field stimuli under different recording conditions (from left to right: isoflurane, *N*=231; FMM, *N*=67; awake, *N*=154; *ex vivo*, *N*=328). Cell classes are color-coded as in Figures 5 and 6 (dark green, monophasic ON; light green, biphasic ON; pink, biphasic OFF; violet, monophasic OFF). ***, *p*<0.001; **, *p*<0.01 (Mann-Whitney *U*-test).

We next explored which neural coding scheme is favorable for awake retinal responses (Supplementary Figure 4; see Methods). Specifically, we first simulated the retinal output responses to a step change in light intensity (e.g., Supplementary Figure 4A,B) using a linear-nonlinear cascade model with the observed temporal filter (STA; Figure 5) and static nonlinear gain function (Figure 6). We then calculated the information based on the simulated peak firing rate ("rate code"; e.g., Supplementary Figure 4C) or response latency ("temporal code"; e.g., Supplementary Figure 4D). We found that the information estimated with the rate code was significantly larger for simulated awake responses (3.4 ± 1.2 bits; median ± interquartile range)

than for anesthetized (isoflurane, 3.0 ± 0.8 bit, p<0.001, Mann–Whitney U-test; FMM, 3.0 ± 0.8 bit, p=0.011) or *ex vivo* responses (2.4 ± 1.3 bit, p<0.001; Supplementary Figure 4E). In contrast, information in the latency-based temporal code of the simulated awake responses (1.9 ± 1.1 bits) was comparable to that of *ex vivo* responses (1.7 ± 1.3 bits, p = 0.6), but significantly lower than those calculated from the simulated anesthetized responses (isoflurane, 2.3 ± 0.6 bits; FMM, 2.4 ± 0.6 bits; both with p<0.001; Supplementary Figure 4F). Here we cannot directly compare the information between the rate and temporal codes as it depends on the assumptions made for the calculation (Eq.(9) in Methods). Nevertheless, information contained in a given coding scheme was calculated under the same assumptions across different recording conditions. Thus, our results suggest that the rate code is in favor of awake responses, while the temporal code is not.

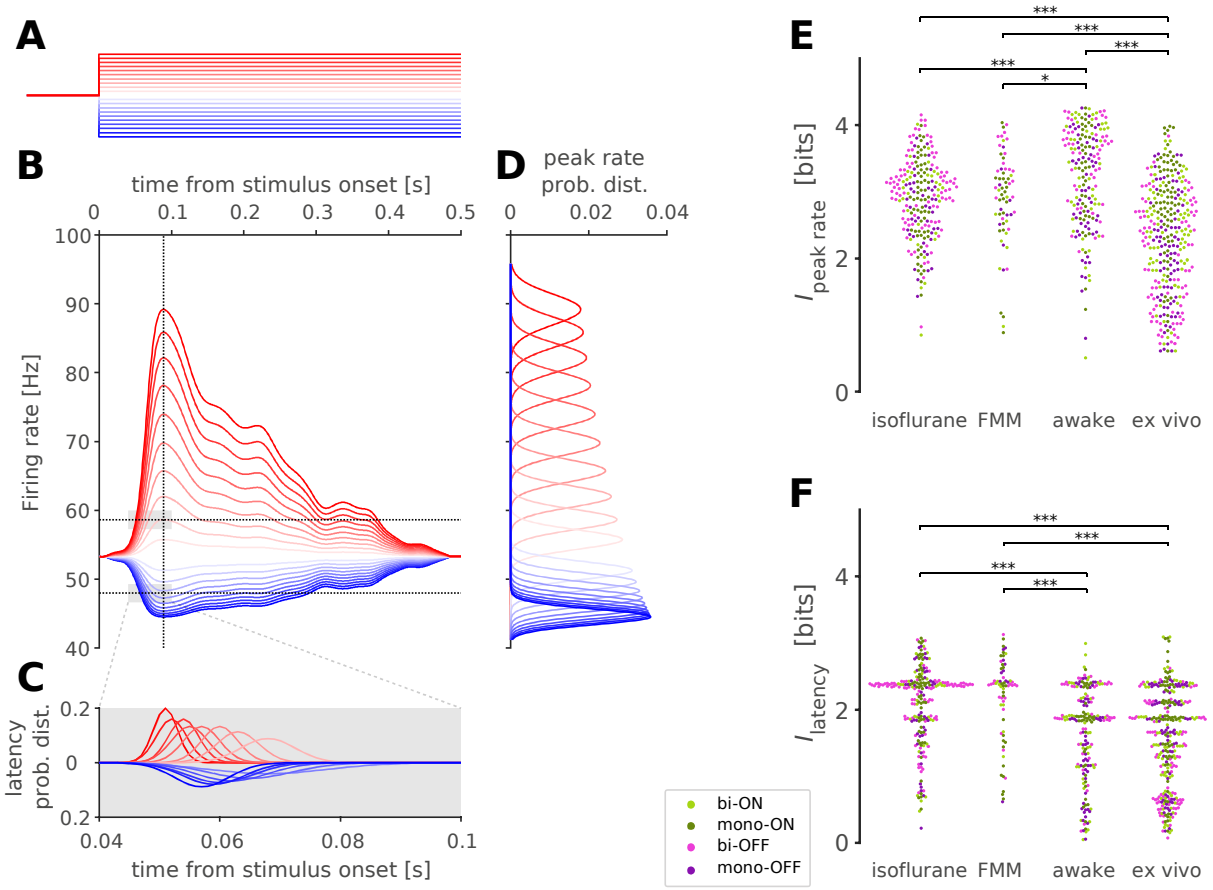

Supplementary Figure 4: Rate coding was more preferable than latency coding for simulated awake retinal responses. *A-D*: Simulated firing rates of a representative awake cell (B) in response to a change in the stimulus contrast at 20 different levels (A, in corresponding colors). The responses were computed from the cell's temporal filter and static nonlinear gain function (see Figures 5 and 6, respectively). The vertical dotted line in B indicates the peak response latency, from which the conditional probability distribution of the peak firing rate, *P*(rate|stimulus), was calculated under the assumption that the standard deviation of the Gaussian distribution follows 2.5% of the peak rates (C). The horizontal lines in B indicate ±10% from the baseline firing rate as the detection threshold to compute the conditional probability distribution of the response latency (D), *P*(latency|stimulus), where the standard deviation of the Gaussian was given by 2.5% of the baseline firing rate (gray shade in B). See Methods for details. *E*: Information in peak rate, $I_{\text{peak rate}}$, in bits computed from *P*(rate|stimulus) as in C for each cell (from left to right: isoflurane, *N*=234; FMM, *N*=67; awake, *N*=195; *ex vivo*, N=328). Cell classes are color-coded as in Figures 5-7 (dark green, monophasic ON; light green, biphasic ON; pink, biphasic OFF; violet, monophasic OFF). ***, $p<0.001$; **, $p<0.01$; *, $p<0.05$ (Mann-Whitney *U*-test). Simulated awake cells have the highest information. *F*: Information in response latency, I_{latency}, computed from *P*(latency|stimulus) as in D for each cell (shown in the same format as E). Given that both increase (red traces in D) and decrease (blue traces in D) of the firing rates are detectable, simulated awake cells have comparable information to cells *ex vivo*, but lower information than those under anesthesia.

Finally, to assess population coding properties, we performed a linear decoding analysis using simultaneously recorded population activity in response to the full-field randomly flickering stimulus (Warland, et al., 1997; see Methods). For each recording session, the performance of the optimized linear decoder was evaluated by Pearson's correlation coefficient, R, between the presented and estimated stimuli with 10-fold cross-validation. For each recording condition, the decoding performance was then examined as a function of the number of simultaneously recorded cells by fitting an exponential saturation function (Eq.(10) in Methods; Figure 8). We found that single-cell linear decoding performance was comparable across recording conditions (awake, $R = 0.20 \pm 0.13$, curve fit parameter a with 95% confidence interval; isoflurane, 0.24 ± 0.04; FMM, 0.24 ± 0.06; *ex vivo*, 0.20 ± 0.10). At the population level, however, Pearson's R reached 0.6 in about a third of the cases in the awake recordings with less than 10 cells to be considered, but none in the anesthetized recordings

with less than 20 cells; and at least ~30 cells were required for the *ex vivo* recordings (Figure 8). Consistent with this observation, the exponential saturation constant was smaller for the awake responses ($b = 8 \pm 4$ from Eq.(10); an estimate with 95% confidence interval) than for the anesthetized (isoflurane, 23 ± 7; FMM, 21 ± 6) or *ex vivo* responses (72 ± 36). This indicates that retinal population responses in awake mice are more linearly decodable than in the other recording conditions, even though an image reconstruction is not necessarily the objective function of the retina.

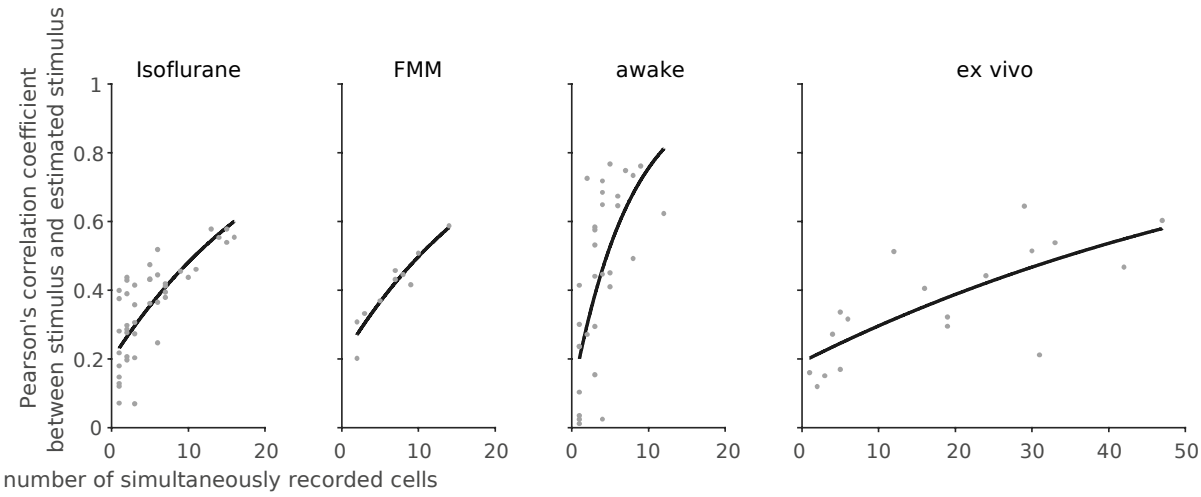

Figure8: Linear decoding of retinal population responses worked best with awake responses. For each recording session, we performed linear decoding of the simultaneously recorded population activity (333 ms window) in response to the full-field randomly flickering stimulus (16.7 ms bin). As a measure of the decoding performance, we then calculated Pearson's correlation coefficient R between the presented and estimated stimuli with 10-fold cross-validation (from left to right: isoflurane, *N*=44; FMM, *N*=10; awake, *N*=33; *ex vivo*, *N*=18). The black line shows the exponential curve fit (Eq.(10) in Methods; isoflurane, $a = 0.23 \pm 0.04$, $b = 23 \pm 7$, estimate with 95% confidence interval; FMM, $a = 0.24 \pm 0.06$, $b = 21 \pm 6$; awake, $a = 0.20 \pm 0.13$, $b = 8 \pm 4$; *ex vivo*, $a = 0.20 \pm 0.10$, $b = 72 \pm 36$).

554 # Discussion

555 Here we established optic tract recordings in head-fixed mice (Figure 1) and systematically
556 analyzed the retinal output properties *in vivo* using a standardized set of visual stimuli for
557 characterizing retinal functions in a high-mesopic / low-photopic regime (Baden et al., 2016;
558 Jouty et al., 2018). We found that awake response properties were overall similar to those
559 under isoflurane or FMM anesthesia (Figures 2-4) or *ex vivo* (Figures 5 and 6); however, we
560 identified three distinct features in the awake condition besides behavioral effects
561 (Supplementary Figures 1 and 2; Schröder et al., 2020): higher firing rates, a larger dynamic
562 range (Figures 3 and 6; Supplementary Figure 3) and faster response dynamics (Figures 4
563 and 5). These properties made the awake responses less efficient from an information
564 theoretic viewpoint (Figure 7 and Supplementary Figure 4) but more linearly decodable at the
565 population level (Figure 8). Our results highlight that our knowledge on retinal physiology
566 cannot be simply translated from *ex vivo* to *in vivo* conditions, and that *in vivo* studies are
567 indispensable to better understand retinal computation.

568 In awake animals, both the baseline and visually-evoked firing rates of RGCs were
569 much higher—on average by ~20 Hz—than in those under anesthesia or in an isolated
570 preparation (Figures 3 and 6). To our knowledge, spiking activity of RGCs in awake mice has
571 been reported only in some recent studies with a low sample size and none of them provided
572 any descriptive statistics (Hong et al., 2018; Schröder et al., 2020; Sibille et al., 2022).
573 Nevertheless, the reported examples (Fig. 3C, Schröder et al., 2020; Fig. S7h, Sibille et al.,
574 2022) show high baseline activity (>10 Hz), consistent with our observation. These two studies
575 employed high-density electrodes (NeuroPixels) to record axonal signals of RGCs in
576 C57BL/6J mice, and are thus arguably comparable to our study from a methodological
577 viewpoint. In contrast, using mesh electrodes directly injected into the mouse eye, Hong et al.
578 (2018) reported relatively low light-evoked RGC responses (<10 Hz) in albino CD1 strain. This
579 is likely not due to the difference in the recording methods, but due to the mouse strain. Albino
580 mice generally have poor vision with a reduced number of rod photoreceptors (Abdeljalil et al.,

2005; Brown et al., 2007), suggesting a certain level of deficits in their retina. High firing activity in awake animals has been widely observed in many brain areas across species (Greenberg et al., 2008; Sellers et al., 2015; Durand et al., 2016; Wright et al., 2017; De Franceschi and Solomon, 2018; Chen and Song, 2019). Therefore, it could be a general feature of the brain in an awake state, including the retina.

This high firing activity had three consequences on the retinal output properties. First, by definition it leads to a lower DS/OS index value calculated as a normalized population vector (Eq.(3) in Methods). Indeed, DS/OS cells were rather underrepresented in our awake recordings with high baseline activity (Figures 2 and 3), while overrepresented in our anesthetized recordings as well as in Hong et al. (2018) with low baseline activity. Second, the baseline activity level affected the response kinetics (Figures 4 and 5). The higher the baseline firing is, the higher the conductance of the cell is, hence the shorter the response latency becomes (Zohar et al., 2011; Wang et al., 2014; Durand et al., 2016). Third, the dynamic range was also altered (Figures 3 and 6; Supplementary Figure 3). Indeed, many awake ON cells exhibited an OFF-suppressive response, an emerging feature observed only in those cells with high baseline firing rates (~60 Hz). Here we categorized these cells separately from the other ON cells in our classification analysis (Figure 2). It is, however, unlikely that they form a distinct “cell type” in the retina, even though we cannot deny a possibility that they were previously overlooked due to a different in the recording modality (calcium imaging; Baden et al., 2016) or clustering methods (Jouty et al., 2019). Instead, these cells likely belong to a known cell type, and altered their response properties due to an increased baseline activity in the awake condition. Possible candidate cell types are: transient ON alpha cells (although they have a low baseline firing rate *ex vivo*; Krieger et al., 2017), ON contrast suppressive cells (although a sharp rebound response is missing in the calcium dynamics *ex vivo*; Baden et al., 2016), or suppressed-by-contrast cells (although their high baseline activity is suppressed by both ON and OFF stimuli; Mastronarde, 1985; Tien et al.,

607 2015; Jacoby and Schwartz, 2018). It is interesting to identify the exact cell type of these
608 RGCs and further characterize their function *in vivo* in future studies.

609 What are the mechanisms underlying such differences between *in vivo* and *ex vivo*
610 retinal responses? One possibility is the difference in the physiological states of the retina.
611 Even if *ex vivo* recordings are made under a proper temperature (Vogel et al., 2016; Vlasiuk
612 and Asari, 2021) using a perfusion medium specifically formulated to support isolated retinal
613 tissues (Ames and Nesbett, 1981), there are certain unavoidable differences to the
614 physiological condition *in vivo*. In particular, the retinal pigment epithelium, a key player for the
615 visual cycle and spatial buffering of ions, is often removed in an isolated retinal preparation. A
616 lack of retinal supply can then alter the physiological states of the retinal neurons, potentially
617 leading to a change in their visual response properties.

618 Differences in the input stimulus properties, in contrast, cannot explain our results,
619 even though retinal responses depend a lot on stimulus conditions. For example, the higher
620 the light intensity level is, the higher the temporal frequency sensitivity becomes for *ex vivo*
621 RGC responses (threshold at around 20-30 Hz; Wang et al., 2011) and so does the critical
622 flicker-fusion frequency at the behavioral level (15-40 Hz; Umino et al., 2018; Nomura et al.,
623 2019). Response latencies depend also on the spatial patterns of stimuli as well as their
624 contrast (Bolz et al., 1982; Baccus and Meister, 2002; Sagdullaev and McCall, 2005; Pearson
625 and Kerschensteiner, 2015; Tikidji-Hamburyan et al., 2015). Here we used full-field stimuli at
626 a somewhat lower light intensity level for *in vivo* recordings than for *ex vivo* ones (see Methods
627 for details). Pupillary reflexes in awake animals further decrease the dynamic range of the
628 stimulus impinging on the retina (Hatter et al., 2003). Therefore, higher baseline activity and
629 faster dynamics observed in awake animals cannot be simply attributed to the difference in
630 the stimulus conditions.

631 Finally, when comparing retinal responses across different studies, one cannot ignore
632 a possible effect of sampling bias because visual response dynamics are cell-type specific
633 (van Wyk et al., 2009; Krieger et al., 2017; Ravi et al., 2018; Tengölics et al., 2019). In an

extreme case, delayed ON cells have the response latency slower than other RGC types by hundreds of milliseconds in an isolated mouse retina (Mani and Schwartz, 2017). Response dynamics are also species-specific. For example, ON RGCs show higher baseline activity and faster responses than OFF cells in the macaque (Chichilnisky and Kalmar, 2002) and guinea pig (Zaghloul et al., 2003) retinas, whereas slower in the salamander retina (Gollisch and Meister, 2008), and such asymmetry between ON and OFF dynamics is pathway-specific in the rat retina (Ravi et al., 2018). Moreover, kinetics can vary even for the same cell type, depending on the retinal location (Warwick et al., 2018) or light-adaptation state (Chang and He, 2014; Tengölics et al., 2019). Sampling bias can then skew the results in many different ways. Given that most RGCs project their axons through the optic tract (Ellis et al., 2016; Rosón et al., 2019), we expect that the optic tract recordings employed in this study should have access to most cell types, if not all. Moreover, here we observed a wide range of visual responses (Figure 2), and no apparent difference was found in the STA distributions across different recording conditions (Figure 5). We thus expect that the effects of sampling bias should be minimal on the observed differences between *in vivo* and *ex vivo* retinal response characteristics.

Taken together, our findings indicate that clear differences exist in retinal physiology between *in vivo* and *ex vivo*. This highlights the importance of studying retinal function *in vivo*, especially in the fully physiological awake condition.

Implications on retinal coding *in vivo*

The optic nerve fiber forms an information bottleneck in the early visual system. The human retina, for example, contains $\sim 10^8$ input neurons (photoreceptors) but only $\sim 10^6$ output neurons (RGCs) whose axons make up the optic nerve (Masland, 2012; Sanes and Masland, 2015). The retina has then been assumed to optimize the channel capacity by compressing the visual information as much as possible and conveying signals to the brain using as few spikes as possible (Attneave, 1954; Barlow and Rosenblith, 1961; Laughlin, 2001). This so-

660 called efficient coding hypothesis is supported by both *ex vivo* experimental data and
661 theoretical analyses. Under *ex vivo* conditions, while some RGCs exhibit high firing under
662 certain conditions (Ke et al., 2014; Smeds et al., 2019), many RGCs are silent most of the
663 time and fire spikes at high rates only when their selective stimulus features are presented
664 (Gollisch and Meister, 2010; Baden et al., 2016; Jouty et al., 2018). This sparse RGC response,
665 ensured by low spontaneous activity and strong nonlinearity (Pitkow and Meister, 2012), helps
666 achieve high efficiency and low redundancy in the visual representation of the retina (Doi et
667 al., 2012). Furthermore, efficient coding principles can explain various physiological properties
668 of the retina, such as separation of retinal outputs into multiple cell types (Gjorgjieva et al.,
669 2019), even though it cannot fully account for the retinal function (Schwartz, 2021).

670 The retinal output characteristics we observed *in vivo*, however, provide a different
671 view on the retinal code. First, unlike *ex vivo* conditions, RGCs in awake mice generally
672 showed a high baseline activity with more linearized responses (Figures 3 and 6).
673 Consequently, many awake ON cells primarily encoded light decrements by suppression from
674 high baseline, rather than light increments by activation from low baseline. These cells convey
675 the same information as conventional ON cells do—the more spikes, the higher light
676 intensity—but using much more spikes. Thus, the amount of information transmitted per spike
677 is much lower *in vivo* than *ex vivo* (Figure 7), violating the efficient coding principles. Second,
678 we found less variability in the visual response dynamics across different RGC classes *in vivo*
679 (Figure 5E-H). This suggests that temporal coding framework may not be readily applicable *in*
680 *vivo* as it requires noticeable differences in spike timing patterns or response latencies
681 between two or more channels, such as ON and OFF pathways converging onto ON-OFF
682 RGCs (Gollisch and Meister, 2008). Our modeling analysis indeed demonstrated that awake
683 responses were in favor of a rate code but not a latency-based temporal code (Supplementary
684 Figure 4), and that a linear decoder worked significantly better with the population responses
685 in awake mice (Figure 8), even though an image reconstruction is not necessarily the retina's
686 objective function. These results point out a need to reconsider retinal function *in vivo*.

What are the advantages of such energy-inefficient retinal coding? As shown in our awake recordings, one can gain faster response kinetics (Figure 5) and wider bandwidths (Figure 6). In addition, redundancy in the dense code helps transmit signals accurately even with intrinsically noisy spike trains, as demonstrated by a high performance of a simple linear decoder (Figure 8). These features are all highly beneficial from a behavioral viewpoint—e.g., to detect predators robustly and promptly—and thus worth achieving for survival at an expense of energy cost. Interestingly, dense coding can be a general feature of early sensory processing, as suggested by high baseline firing in vestibular and cochlear nuclei (Fuchs and Kimm, 1975; Rhode and Smith, 1986; Warchol and Dallos, 1990; Beraneck and Cullen, 2007), tonic activity in hair cells (Sachs and Abbas, 1974; Wu et al., 2016), and dark current in vertebrate photoreceptors (Hagins et al., 1970; Okawa et al., 2008). In fact, the energy cost of dense retinal coding may not be so problematic with a relatively small number of neurons, as opposed to the total energy required for operating $\sim 10^9$ neurons in the cortex where sparse coding has certain advantages from the viewpoints of both energy efficiency and sensory processing (Olshausen and Field, 1996; Asari et al., 2006).

The retina, however, may employ different coding principles under different light levels (Wang et al., 2011; Tikidji-Hamburyan et al., 2015; Borghuis et al., 2018). All our *in vivo* recordings were done in a high-mesopic / low-photopic range (at ~10^3 R*/photoreceptor/s; see Methods). In a scotopic condition, in contrast, *ex vivo* studies have reported a high tonic firing rate for OFF RGC types (~50 Hz, OFF sustained alpha cells in mice; Smeds et al., 2019; ~20 Hz, OFF parasol cells in primates; Ala-Laurila and Rieke, 2014), while a low tonic firing for corresponding ON cell types (<1Hz). Since these ON cells were shown to be responsible for light detection by firing in the silent background (Smeds et al., 2019), here the retina seems to operate with a sparse feature detection strategy. Further characterizations of the retinal code *in vivo* and its behavioral relevance will be needed to clarify what exactly the eye tells the brain.

712 # Effects of anesthetics in early visual system

713 Anesthetics generally lower the excitability of nerve cells: e.g., isoflurane acts on the gamma-
714 aminobutyric acid (GABA) type A receptors to silence the brain (Jenkins et al., 1999). It thus
715 makes sense that the retinal outputs were reduced under anesthesia (Figures 3 and 6) and
716 showed slower dynamics (Figures 4 and 5) than in awake animals. It is, however, difficult to
717 generalize the effects of anesthesia because multiple mechanisms of action are involved,
718 exerting complex effects on the sensory systems in anesthetic- and dose-dependent manners
719 (Populin, 2005). For example, while visual cortical responses are reduced under anesthesia
720 (Haider et al., 2013; Vaiceliunaite et al., 2013), auditory responses are enhanced (Raz et al.,
721 2014; Sellers et al., 2015) and the response latency becomes shorter in the auditory pathway
722 (Ter-Mikaelian et al., 2007).

723 Our results are nevertheless consistent with previous studies on the effects of
724 anesthesia in the early visual system. Specifically, anesthesia reduces the overall activity of
725 both SC and dLGN neurons, and leads to multiple changes in temporal processing of these
726 two major retinorecipient areas, such as reduced sensitivity to high temporal frequencies and
727 longer response latencies (Zhao et al., 2014; Durand et al., 2016; De Franceschi and Solomon,
728 2018). While different anesthetics were used in these studies (urethane as opposed to
729 isoflurane and FMM), our consistent findings suggest that such changes in the response
730 dynamics arise largely from the retina. In contrast, the effects of anesthesia on spatial
731 response properties seem more complex. While spatial processing remains largely intact in
732 dLGN (Durand et al., 2016), lower sensitivity to contrast and larger receptive field sizes were
733 reported in SC under urethane anesthesia (De Franceschi and Solomon, 2018). Moreover,
734 SC neurons show increased orientation selectivity under isoflurane anesthesia (Kasai and Isa,
735 2021). Here we also found a larger fraction of DS/OS cells under both isoflurane and FMM
736 anesthesia than in the awake condition (Figure 2D-F). This, however, could be due to the
737 difference in the baseline firing rate (Figure 3) as the DS/OS index is defined by a normalized

population vector in response to moving gratings (Eq.(3). In Methods; Mazurek et al., 2014). It is a future challenge for fully characterizing spatiotemporal processing of the retina *in vivo*.

Materials and Methods

No statistical method was used to predetermine the sample size. The significance level was 0.05 (with Bonferroni correction where appropriate) in all analyses unless noted otherwise. All experiments were performed under the license 233/2017-PR from the Italian Ministry of Health, following protocols approved by the Institutional Animal Care and Use Committee at European Molecular Biology Laboratory. The data analyses were done in Python.

Animals

A total of 55 female C57BL/6J mice were used (chronic, 3; acute, 35; failures, 17, including 10 initial unsuccessful attempts to record from the optic chiasm) at around three months of age at the time of the surgery. Mice were kept on a 12-h light / 12-h dark cycle and given water and food *ad libitum*. After the chronic implantation of electrodes, the animals were kept single-housed.

Chronic recordings

For implanting electrodes, animals were anesthetized (induction, 4% isoflurane; maintenance, 1-2%) and placed inside a stereotaxic apparatus (Neurostar). Throughout the surgery, temperature was maintained at 37 °C using a heating pad (Supertech Physiological), and eye ointment (VitA-POS) was used to prevent the eyes from drying. After positioning the mouse head, the scalp skin was disinfected (Betadine) and removed with scissors. Soft tissue was removed from the skull surface with a round scalpel, and ethanol and acetone were applied to the skull for disinfection and removal of any residual compounds. The skull was glazed with a drop of cyanoacrylate adhesive (Loctite 401) to secure in place the surrounding skin, and then registered in the stereotaxic controller software (NeuroStar). A dental drill (WPI) was used to leave three marks on the skull to label the entry point for targeting the optic tract: [-1.34, +1.87,

763 +4.74], [-1.70, +1.87, +4.74], and [-1.82, +2.35, +4.07] in [Anterior-Posterior, Medial-Lateral,
764 Dorsal-Ventral] coordinates, respectively. A hole was drilled for a reference silver wire (A-M
765 Systems) above the cerebellum, and the wire was inserted sideways to avoid excessive brain
766 damage. After covering the hole and wire with Vaseline, the wire was attached to the skull
767 with cyanoacrylate adhesive and dental cement (Paladur, PALA). Subsequently, a custom-
768 designed titanium head-plate was attached to the skull with dental cement, followed by a
769 craniotomy (diameter, 1-2 mm) and durotomy. A chronic silicone probe (Buzsaki32L,
770 NeuroNexus) was then inserted with the stereotaxic controller (75 μm/min) first to a depth of
771 2 mm, retracted by 1 mm to release pressure created by the initial brain entry, and then to a
772 depth of 4.5 mm from the skull surface. After reaching the desired depth, a microdrive (dDrive,
773 NeuroNexus) was attached to the skull with dental cement, and the probe was removed from
774 its mount and covered with a protective cap. The cables and connectors were cemented to
775 the cap and covered with paraffin film (Bemis, Parafilm) to prevent the mouse from damaging
776 the implant.

777 After the surgery, the animals were kept on a heating pad (Sera, Thermo comfort mat
778 S) until they recovered from anesthesia. During the next four days, the mice received an anti-
779 inflammatory/antibiotic cocktail (Rimadyl/Baytril; 0.5 mg/mL each, 0.01 mL/g). The antibiotic
780 (Baytril) was given for an additional three days through drinking water (0.17 mg/mL).

781 After a recovery period of five days, the mice were placed on a custom-made rotary
782 treadmill (diameter, 20 cm) with their head fixed for the recordings (at most two times a day,
783 each for <2 hours). During the initial sessions, we moved the probe until visual responses
784 were observed (Figure 1A-D). The electrophysiology data were recorded at 30 kHz from each
785 recording site (SmartBox, NeuroNexus) together with synchronization pulses from the visual
786 stimulation device (see below). In total, we made 17 recording sessions from 3 out of 6 animals,
787 where up to 10 cells were simultaneously recorded in each session (4.4 ± 2.4 cells/session,
788 mean ± standard deviation).

789 After all the recording sessions, the electrode position was verified histologically (e.g.,
790 Figure 1E). The mice were anesthetized (2.5% Avertin, 16 μL/g, intraperitoneal injection) and
791 perfused with paraformaldehyde (PFA; 4% in phosphate buffer solution). The animal's head
792 with the electrode left in position was collected without the skull base, and stored in fixative
793 solution (4% PFA) at 4°C for at least four days. This helped the brain tissue harden around
794 the silicon probe, hence leaving a visible mark after removing the probe. Harvested brain
795 tissue was then coronally sliced with a vibratome (Leica, VT1000S; thickness, 150 μm) and
796 imaged under a bright-field microscope (Leica, LMD7000).

797 Acute recordings

798 Animals were anesthetized and placed inside a stereotaxic apparatus with a heating pad as
799 described above. A contact lens (diameter, 3 mm; Ocuscience) was used for the target eye to
800 prevent it from drying. The scalp was removed, registered in the stereotaxic controller, and
801 the three entry points for targeting the optic tract were marked with the stereotaxic drill. A well
802 was made with dental cement around the marks later to hold saline solution on top of the brain.
803 After a craniotomy (diameter, 2 mm), an acute silicone probe (Buzsaki32L, Neuronexus)
804 coated with a fluorescent dye (DiI stain, Invitrogen, D282) was slowly inserted into the brain
805 (100 μm/min) with a micromanipulator (Sensapex, SMX) attached to the stereotaxic apparatus.
806 While approaching the target depth, visual stimuli were presented (full-field contrast-inverting
807 stimulus at 0.5 Hz; see below). The probe was moved until a maximum number of visually
808 responsive cells were seen at once (up to 20 cells; 7.7 ± 5.3 cells/session, mean ± standard
809 deviation; 52 sessions in total from 23 out of 27 animals).

810 Throughout the recordings, the mouse was kept under anesthesia with 1% isoflurane.
811 The depth of anesthesia was monitored by the breathing rate (~1 breath/s). Alternatively, we
812 used a cocktail of fentanyl, medetomidine and midazolam (FMM) during the recordings. In this
813 case, once the electrode was in position, an FMM solution (fentanyl, 0.05 mg/kg;
814 medetomidine, 0.5 mg/kg; midazolam, 5 mg/kg; in 0.9% NaCl saline) was intraperitoneally
815 administered, and the isoflurane dose was progressively decreased to 0%. Buprenorphine

816 (0.1 mg/kg) was injected 20 minutes after the termination of isoflurane, and the recording
817 session was initiated 10 minutes after the buprenorphine injection. The depth of anesthesia
818 was monitored through the heart rate (below around 300 beats per minute) and supplemental
819 FMM anesthesia was provided when required. The electrophysiology data and the visual
820 stimulation signals were recorded at 30 kHz/electrode (SmartBox, NeuroNexus).

821 At the end of the recording session, the electrode location was verified histologically.
822 After retracting the silicone probe, the animal was perfused as described above. The brain
823 tissue was harvested and post-fixed overnight in 4% PFA at 4°C. Coronal sections of the brain
824 tissue (thickness, 150 μm) were then examined under a fluorescence microscope (Leica,
825 LMD7000 with N2.1 filter cube) to visualize the trace left by the DiI stain on the probe.

826 For acute awake recordings, we first performed head-plate implantation as described
827 above. In short, after placing an animal on a stereotaxic apparatus under anesthesia, we 1)
828 surgically removed the skin and the periosteum above the skull; 2) attached a head-plate to
829 the skull with dental cement; and 3) applied a thin layer of cyanoacrylate adhesive (Loctite
830 401) and a thick layer of silicone sealant (Kwik-cast) to provide mechanical and thermal
831 support. Animals were then allowed to recover for a week, and subsequently habituated over
832 the course of 10 days to head fixation in the recording setup as described above. On the day
833 of the recording, we removed the silicone to expose the skull surface of the animal with its
834 head fixed in the recording setup, and determined the electrode penetration path to the target
835 area using the robotic stereotaxic system (StereoDrive, NeuroStar). The animal was then
836 briefly anesthetized (for about 5 minutes) and a hole was drilled around the electrode entry
837 point on the skull. After the removal of the anesthesia, the electrode attached to the robotic
838 arm was lowered at 5 μm/s until visual responses were found in the target area. Recordings
839 and histological verification of the electrode location were performed as described above.

840 # Visual stimulation

841 Visual stimuli were presented by a custom gamma-corrected digital light processing (DLP)
842 device (Texas Instruments, DLPDLCR3010EVM-LC) where the original green and red light-
843 emitting diodes (LEDs) were replaced with ultra-violet (UV; 365 nm; LZ1-00UV00, LED
844 Engine) and infrared (IR; 950 nm; SFH 4725S, Osram) LEDs, respectively. The UV and blue
845 (465 nm) lights were projected onto a spherical screen (radius, 20 cm) with UV-reflective white
846 paint (waterfowl store) placed ~20 cm to the contralateral side of an animal's eye from the
847 implanted probe (Figure 1A), whereas the IR light was used as synchronization pulses,
848 recorded via a photodiode with a custom transimpedance amplifier. The visual stimuli (1280-
849 by-720 pixels; frame rate, 60 Hz) covered $\omega_{azimuth}$ = 73° in azimuth and $\omega_{azimuth}$ = 44° in altitude
850 from the mouse eye position (Figure 1B). The maximum light intensity at the eye position was
851 31.3 mW/m^2 (E_{365} = 15.4 mW/m^2 for UV LED and E_{365} = 15.9 mW/m^2 for blue LED; measured
852 with S121C sensor, Thorlabs), leading to mesopic to photopic conditions (see also "Light
853 intensity" section below).

854 Using this DLP setup and QDSpy software (Franke et al., 2019), we presented the
855 following set of visual stimuli: a randomly flickering full-field stimulus (5 min; 60 Hz), a moving
856 grating stimulus (spatial frequencies of square waves, 3° or 20°; moving speed, 7.5°/s or 15°/s,
857 in eight different directions), a full-field stimulus whose intensity followed a sinusoid (1.5 Hz)
858 with a linearly increasing amplitude from 0% to 100% contrast over 10 s (10 trials; Figure 3),
859 and a full-field sinusoidally flickering stimulus (maximum contrast) at different temporal
860 frequencies (1.875, 3.75 and 7.5 Hz, each for 2 s; 15 Hz for 1 s; 10 trials; Figure 4). The last
861 two full-field stimuli were preceded by a sequence of "OFF-ON-OFF" stimulation at maximum
862 contrast (full-field contrast inversion; 2 s each) and interleaved by a 1-s-long gray screen
863 across trials. These stimuli were equivalent to those used for differentiating ~30 RGC types
864 *ex vivo* (Baden et al., 2016; Jouty et al., 2018).

Light intensity

We calculated the photon flux on the mouse retina in vivo as: $I_\lambda = T_\lambda \cdot F_\lambda \cdot A_{pupil}/A_{retina}$, where T_λ is the transmittance of the eye optics at wavelength λ; $F_\lambda = E_\lambda/(hc/\lambda)$ is the photon flux at the pupil with Planck's constant h and the speed of light c; $A_{pupil} \approx \pi \cdot (d_{pupil}/2)^2$ is the pupil area with diameter d_{pupil}; and $A_{retina} \approx (\pi \cdot d_{retina} \cdot \omega_{azimuth}/360°) \cdot (\pi \cdot d_{retina} \cdot \omega_{azimuth}/360°)$ is the illuminated retinal area with diameter d_{retina}. Assuming that T_{365} = 50%, T_{454} = 68% (Jacobs and Williams 2007), d_{pupil} = 1 mm and d_{retina} = 4 mm, we then obtained $I_{365} = 3.81\times10^3$ and $I_{454} = 6.64\times10^3$ photons/s/μm^2. Given a total photon collecting area a = 0.2 and 0.5 μm^2 for cones and rods, respectively (Nikonov et al., 2006), and a relative sensitivity s_{365} = 90% and s_{454} = 0% for S-cones while s_{365} = 25% and s_{454} = 60% for M-cones and rods (Jacobs and Williams 2007), we estimated the photoisomerization (R*) rate as: $a \cdot \Sigma_\lambda I_\lambda s_\lambda = 2.5\times10^3$ R*/rod/s, 0.7×10^3 R*/S-cone/s, and 1.0×10^3 R*/M-cone/s.

In contrast, the maximum light intensity of the *ex vivo* set up was E = 36 mW/m^2 (Vlasiuk and Asari, 2021). Assuming that the white light from a cathode-ray tube monitor is centered around λ = 500 nm, we estimated the photon flux on an isolated retina as: $I = E/(hc/\lambda) = 9\times10^4$ photons/s/μm^2. Given the sensitivity s_{500} = 2% for S-cones and 40% for M-cones and rods (Nikonov et al., 2006), we then obtained: $a \cdot I \cdot s_{500} = 4\times10^4$ R*/rod/s, 2×10^3 R*/S-cone/s, and 4×10^4 R*/S-cone/s. Thus, the light intensity level was about an order of magnitude higher for *ex vivo* data than for *in vivo* data.

Physiology data analysis

In total, we obtained 282 cells in awake conditions (75, chronic; 282, acute), and 325 and 103 cells in acute anesthetized recordings with isoflurane and FMM, respectively. Spike sorting was performed with SpykingCircus (Yger et al., 2018) for semi-automatic cluster detection and Phy (Rossant, 2020) for data curation. In brief, spikes were detected from highpass-filtered data traces (cutoff, 300 Hz) as those events 7 standard deviations away from the mean. Single-units were then identified by clustering in principal component space, followed by

manual inspection of spike shape as well as auto- and cross-correlograms. As expected from axonal signals (Barry, 2015), spike waveforms typically had a triphasic shape (e.g., Figure 1F-H). No putative single-units had the interspike intervals below 1 ms for a refractory period (e.g., Figure 1I-K), except for 1 (out of 103) for FMM-anesthetized recordings. Most units had a minimum interspike interval above 2 ms (93%, awake; 94%, isoflurane; 99%, FMM). Here we included in the analysis those small numbers of visually responsive cells that had a small fraction of interspike intervals below 2 ms; removing them did not affect the conclusions. Not all cells responded to the entire stimulus set, but cells responding to any of the presented stimuli were included in the analysis.

For *ex vivo* recordings, we reanalyzed the data sets in Vlasiuk and Asari (2021). Specifically, the *ex vivo* data sets included the activity of 696 cells recorded with a multi-electrode array (from 18 isolated mouse retinas) in oxygenated Ames' medium at 37 °C in response to a randomly flickering full-field visual stimulus projected from a gamma-corrected cathode-ray tube monitor (frame rate, 100 Hz) or a DLP device (60 Hz). Given that the temperature of the ocular surface is ~37 °C (Vogel et al., 2016), the retina likely operates at around 37 °C *in vivo*.

Response quality

We assessed the cell's response quality based on the trial-to-trial reliability of the response $r(t)$ during the "ON-OFF" period of the OFF-ON-OFF stimulus sequence (see Figure 2A for example). Specifically, the signal-to-noise ratio was calculated for each cell as follows:

$$\mathrm{SNR} = \frac{\mathrm{var}[\langle r(t) \rangle]_t}{\langle \mathrm{var}[r(t)]_t \rangle}, \tag{1}$$

where $\langle \cdot \rangle$ indicates the mean over trials, and $\mathrm{var}[\cdot]_t$ the variance over time t (bin size, $\Delta t = 16.6$ ms). We set a threshold at 0.15 to select reliably responsive cells for further analyses (Figure 2B).

Response polarity

To characterize the cell's preference to stimulus polarity, we defined an ON-OFF index using the responses to the full-field contrast inversion:

$$\text{ON-OFF index} = \frac{r_{\text{ON}} - r_{\text{OFF}}}{r_{\text{ON}} + r_{\text{OFF}}}, \tag{2}$$

where r_{ON} and r_{OFF} are the mean firing rate during the ON and the second OFF periods of the OFF-ON-OFF stimulus sequence, respectively. Positive and negative ON-OFF index values indicate stronger responses to ON and OFF stimuli, respectively (Figure 2C).

Direction and orientation selectivity

Direction-selectivity (DS) and orientation-selectivity (OS) indices were calculated by projecting the responses to the moving grating stimuli onto a complex exponential (Mazurek et al., 2014):

$$\text{DS or OS index} = \left\| \frac{\sum_k e^{-i\alpha\omega_k} \cdot r_k}{\sum_k r_k} \right\|, \tag{3}$$

where ω_k and r_k are the angle of the k-th direction and the cell's corresponding responses, respectively; and $\alpha = 1$ and 2 for the DS and OS indices, respectively. Cells were considered DS and/or OS when the corresponding index was higher than 0.15 and $p < 0.2$ calculated by bootstrap methods (1,000 repetitions; Figure 2D-F).

Temporal frequency sensitivity

Temporal frequency sensitivity was assessed by fitting an even power of sine function to the responses to the full-field sinusoidally flickering stimulus at different frequencies h (1.875, 3.75, 7.5, or 15 Hz; Figure 4):

$$s(t) = A \cdot \sin^q\left(\pi h t - \frac{\phi}{2}\right) + B, \tag{4}$$

where A and $B \geq 0$ are the evoked response amplitude and baseline activity, respectively; and $q = 2n$ with $n \in \mathbb{N}^+$ is the exponent of the sine function. The phase $\phi \in [-\pi, \pi)$ indicates the relative position between the response peak and the sinusoidal stimulus patterns. For example,

$\phi = -\pi/2$ and $\pi/2$ are obtained if the response reaches its peak when the stimulus is brightest and darkest, respectively.

The fit quality was then assessed by the explained variance:

$$R^2 = 1 - \frac{\mathrm{var}[\mathrm{Data} - \mathrm{Fit}]}{\mathrm{var}[\mathrm{Data}]}. \tag{5}$$

We set a threshold at 0.2 to select cells with a good fit hence responsive to the stimulus (Figure 4C), and compared the proportions of the responsive cells across different recording conditions (two-proportion z-test; Figure 4C,D).

Sensitivity to contrast

We used an even power of sine function with a sigmoid envelope to characterize the responses to the flickering stimulus ($h = 1.5$ Hz) with increasing contrast (Figure 3):

$$S(t) = \frac{A}{1 + e^{-\lambda(t - t_0)}} \cdot \sin^q\left(\pi h t - \frac{\phi}{2}\right) + B, \tag{6}$$

where t_0 and $\lambda > 0$ are the midpoint and the steepness of the sigmoid, respectively; and the other free parameters are the same as $s(t)$ in Eq.(4). The fitted parameter values were then compared across different recording conditions: Mann-Whitney U-test for the baseline B (Figure 3D) and the absolute amplitude $|A|$ (Figure 3E), and t-test for the phase ϕ for ON and OFF responses, respectively (*k*-means clustering with *k* = 2; Figure 3F). As a measure of the sensitivity to contrast, we used an estimated response magnitude at 10% contrast from Eq.(6) as well as the absolute slope size at the midpoint of sigmoid ($|A\lambda/4|$).

Temporal filters and static nonlinear gain functions

For systematically characterizing the response dynamics, we used stimulus ensemble statistical techniques ("reverse correlation" methods; 500 ms window) to calculate the linear filter (Figure 5) and static nonlinear gain function (Figure 6) of the recorded cells in response to a randomly flickering visual stimulus (Meister et al., 1994; Chichilnisky, 2001). First, we obtained the linear filter of each cell by calculating a spike-triggered average (STA) of the

stimulus with ± 1 being "white" and "black," respectively. As a quality measure, p-value was computed for each time bin against a null hypothesis that the STA follows a normal distribution with a mean of zero and a variance of $1/C$, where C is the total number of spikes. As a measure of the cell's temporal frequency tuning, we then estimated the peak latency by fitting a difference-of-Gaussian curve to the linear filter (e.g., Figure 5A); and the spectral peak frequency by the Fourier analysis on the fitted curve (e.g., Figure 5B). The curve fitting quality was assessed by the explained variance R^2 as in Eq. (5). We discarded the cells if $p > 10^{-18}$ for all time bins or $R^2 < 0.8$. We ran a t-test to compare the temporal frequency tuning properties at the population level across recording conditions (Figure 5C,D) or across different cell types in each recording condition (Figure 5E-H). Spatial response properties were not examined in this study because complex nonlinear kinematics of eye movements in the awake condition precluded the analysis at a high enough spatial resolution; and because it has been shown that anesthesia has no effect on the spatial processing in dLGN, a direct downstream of the retina (Durand et al., 2016).

Static nonlinear gain function $P(\text{response}|\text{stimulus})$ of each cell was computed by taking the ratio between the distribution of spike-triggered stimulus ensembles $N(\text{stimulus}|\text{response})$ projected onto the $L2$-normalized STA (bin size, 0.1) and that of the entire stimulus ensembles $N(\text{stimulus})$ (e.g., Figure 6B):

$$P(\text{response}|\text{stimulus}) = \frac{N(\text{stimulus}|\text{response})}{N(\text{stimulus})} / \Delta t\,. \tag{7}$$

A sigmoid function was fitted to $P(\text{response}|\text{stimulus})$ for smoothing. The neutral stimulus response was then defined as the vertical-intercept of the sigmoid function at the horizontal axis value of zero: i.e., the firing rate when the stimulus is orthogonal to the STA. We ran a t-test to compare the neutral stimulus responses and the average firing rates during the stimulus presentation at the population level across conditions (Figure 6A,C); and Mann-Whitney *U*-test to compare the midpoint of the sigmoid (Figure 6H). The dynamic range was computed

for each cell as the difference between the maximum and minimum firing rates of the static nonlinear gain function (Supplementary Figure 3).

Response classification

In this study, we were not able to perform a morphological analysis of individual cells as we employed blind *in vivo* recording methods (Figure 1). We thus focused on the visual response properties for categorizing cell-classes in the following two ways.

First, we classified cells *in vivo* using the response quality, response polarity, and motion sensitivity (Figure 2). Specifically, we first divided the cells into two groups: reliably responsive ones with $\mathrm{SNR} > 0.15$ (Eq. (2)) and the other low quality ones ("N/A" type; Figure 2B). We then set thresholds at ± 0.25 for the ON-OFF index (Eq. (3)) to identify ON, OFF, and ON/OFF cells within the reliably responsive cells that increased firing in response to light increments, light decrements, and both, respectively (Figure 2C). For some cells where these measures were not available, we used the responses to the full-field sinusoidally flickering stimuli to calculate the response quality and polarity in a similar manner. Within the ON cells, we further identified an "OFF-suppressive" class if they had a significant negative amplitude in Eq. (6) with 95% confidence intervals in the parameter estimation. Independently, we also labeled cells as motion sensitive or not, based on the DS/OS indices as described above (Eq.(3); Figure 2D-F).

Second, because these measures are not available for the *ex vivo* data sets (Vlasiuk and Asari, 2021), we performed classification using the temporal filter properties to make a fair comparison between the *ex vivo* and *in vivo* data sets (Figures 5 and 6). Specifically, we first ran a principal component analysis (PCA) on the temporal filters ($L2$-normalized STA) obtained in each condition (Gollisch and Meister, 2008; Asari and Meister, 2014). The first two principal components (PC1, monophasic filter; and PC2, biphasic filter) were largely sufficient to fit all the temporal filter dynamics, accounting for 78-86% of the total variance in each condition. Each temporal filter is a point in the PCA biplot (i.e., the two-dimensional space

1013 spanned by PC1 and PC2), and we grouped its shape into four subtypes based on its position:
1014 monophasic OFF, biphasic OFF, monophasic ON, and biphasic ON from the first to the fourth
1015 quadrants, respectively.

1016 Here we did not aim to fully differentiate all functional cell-types (~35 RGC types from
1017 *ex vivo* studies; Baden et al., 2016; Jouty et al., 2018) for three reasons. First, our data sets
1018 are not large enough. Second, the presented stimulus sets were not diverse enough. Finally,
1019 some cells may have not been sampled, such as those projecting to the ipsilateral side of the
1020 brain, or those projecting exclusively via the retinohypothalamic tract (e.g., to the medial
1021 terminal nucleus of the accessory optic system; Yonehara et al., 2009; Gauvain and Murphy,
1022 2015). Thus, here we did not use the term “cell-type” to avoid confusion.

1023 Behavior data analysis

1024 We monitored the behavioral states of an animal during *in vivo* recordings in two ways
1025 (Supplementary Figure 1). First, we monitored the running speed based on the turning speed
1026 of the custom-made rotary treadmill. Second, we videotaped the animal’s eye, facing towards
1027 the visual stimulation screen. Eye tracking was done by passing individual frames of the eye
1028 videos to Mask R-CNN, an object detection and segmentation neural network (He et al., 2017;
1029 Abdulla, 2017). Mask R-CNN was fine-tuned with 500 manually annotated frames of our
1030 recordings, covering the range of pupil size and background illumination found in our setup.
1031 The detected masks were fitted with an ellipse, retrieving the center coordinate, semi-major
1032 and -minor axes, and rotation angle (e.g., Supplementary Figure 1A).

1033 Pairwise cross-correlation (100 ms bin) was calculated between the RGC firing rate,
1034 running speed and pupil size (Supplementary Figure 2) for the recording period where the
1035 mean light intensity was relatively stable: i.e., randomly flickering full-field stimulation and
1036 moving grating stimulation periods. The peak value was then selected within 5 s lag while the
1037 p-value was calculated from the data outside the range. The peak cross-correlation was

similarly calculated between the pupil size and the light intensity for the full-field sinusoidally flickering stimulus and the full-field contrast inversion stimulation periods.

Model analysis

Information theoretic analysis

We took an information theoretic approach to quantify the amount of information carried by the retinal output spike trains (Figure 7; Rieke et al., 1997), focusing on the randomly flickering full-field stimulation period (T = 300 s). Specifically, we calculated the information conveyed by a single spike, I_{spike} bits/spike, using the following formula:

$$I_{\text{spike}} = \frac{1}{T}\int_0^T dt \left[\frac{r(t)}{\bar{r}}\right] \log_2 \left[\frac{r(t)}{\bar{r}}\right], \tag{8}$$

where $r(t)$ is the instantaneous firing rate of a target cell using small time bins Δt, and $\bar{r}$ is the average firing rate over time. To avoid the estimation bias due to the finite data size, we computed I_{spike} in Eq.(8) as a function of bin size Δt, performed a linear regression to the well-behaved linear portion of these measurements, and extrapolated to the limit $\Delta t \to 0$ (i.e. the y-intercept). The information rate conveyed by a target cell was then given as: $I_{\text{rate}} = \bar{r} \cdot I_{\text{spike}}$ bits/s.

Rate and latency coding models

We took a modeling approach to examine how retinal coding is affected by the response characteristics observed under different recording conditions (Supplementary Figure 4; Gollisch and Meister, 2008). Specifically, using the temporal filter (STA; Figure 5) and static nonlinear gain function (Eq.(7); Figure 6) in the linear-nonlinear cascade model framework, we first simulated the responses of each cell to a step change in light intensity at 10 different levels of contrast increase and decrease, respectively (n_{level} = 20 in total; e.g., Supplementary Figure 4A,B). To estimate the information contained in a given characteristic x of the simulated responses, we then used the following formula:

$$I = \sum_s \int dx\, p(s)\, p(x|s)\, \log_2 \frac{p(x|s)}{p(x)}, \tag{9}$$

where $p(s) = 1/n_{\text{level}}$ is the probability of the stimulus s; $p(x|s)$ is the conditional probability density of x given stimulus s; and $p(x) = \sum_s p(s)\, p(x|s)$ is the total probability density of x, obtained as the normalized sum of $p(x|s)$. For rate coding (Supplementary Figure 4E), we focused on the peak firing rate of the simulated responses, and assumed that $p(x = \text{"peak rate"} \mid s)$ follows a Gaussian distribution with the mean and standard deviation of the peak firing rate and its 2.5% value, respectively (e.g., Supplementary Figure 4C). For temporal coding (Supplementary Figure 4F), we focused on the response latency, where we assumed that the detection threshold was given by 10 ± 2.5% deviation from the baseline firing rate (mean ± standard deviation of a Gaussian distribution), from which $p(x = \text{"latency"} \mid s)$ was calculated (e.g., Supplementary Figure 4D). For stimuli that did not trigger strong enough responses to cross the detection threshold, the response latency was considered to be infinity.

Linear decoding model

We used a linear decoding model to investigate how population coding of the retina depends on the recording conditions (Figure 8). Specifically, we first computed the optimal linear decoder (333 ms window with a bin size of 16.7 ms) from the simultaneously recorded population activity in response to the full-field randomly flickering stimulus (Warland, et al., 1997). The performance of the linear decoder was measured by Pearson's correlation coefficient between the presented and estimated stimuli with 10-fold cross-validation. For each recording condition, the decoding performance as a function of the number of input cells, n, was then assessed by fitting the following exponential saturation function with a plateau at 1:

$$f(n) = 1 - (1 - a)e^{-(n-1)/b}, \tag{10}$$

where $a = f(1) \in [0, 1]$ represents the single-cell decoding performance; and $b > 0$ is the saturation constant, hence a larger value of b indicates that the linear decoding requires a larger population to improve its performance.

Acknowledgments

This work was supported by research grants from EMBL (H.A.). The EMBL Histology Facility and the Advanced Light Microscopy Facility are acknowledged for support in sample preparation and image acquisition for histological analyses, respectively. EMBL IT Support is acknowledged for provision of computer and data storage servers; and the LAR facility for taking care of animals. We thank Dmitry Molotkov for his help in setting up the recording rig, and all the Asari lab members as well as Cornelius Gross and Santiago Rompani for many useful discussions.

References

Abdeljalil, J., Hamid, M., Abdel-Mouttalib, O., Stéphane, R., Raymond, R., Johan, A., José, S., Pierre, C., Serge, P. (2005). The optomotor response: a robust first-line visual screening method for mice. Vision Res, 45(11), 1439-1446.

Abdulla, W. (2017). Mask R-CNN for object detection and instance segmentation on Keras and TensorFlow. GitHub repository, https://github.com/matterport/Mask_RCNN

Ala-Laurila, P., Rieke, F. (2014). Coincidence detection of single-photon responses in the inner retina at the sensitivity limit of vision. Curr Biol, 24(24), 2888-2998.

Ames, A., Nesbett, F. B. (1981). In Vitro Retina as an Experimental Model of the Central Nervous System. J Neurochem, 37(4), 867-877.

Asari, H., Meister, M. (2014). The projective field of retinal bipolar cells and its modulation by visual context. Neuron, 81(3), 641-652.

Asari, H., Pearlmutter, B. A., Zador, A. M. (2006). Sparse representations for the cocktail party problem. J Neurosci, 26(28), 7477-7490.

Atick, J. J., Redlich, A. N. (1990). Towards a Theory of Early Visual Processing. Neural Comput, 2(3), 308-320.

Attneave, F. (1954). Some informational aspects of visual perception. Psychol Rev, 61(3), 183-193.

Baccus, S. A., Meister, M. (2002). Fast and slow contrast adaptation in retinal circuitry. Neuron, 36(5), 909-919.

Baden, T., Berens, P., Franke, K., Rosón, M. R., Bethge, M., Euler, T. (2016). The functional diversity of retinal ganglion cells in the mouse. Nature, 529(7586), 345-350.

Barlow, H. B., Hill, R. M., Levick, W. R. (1964). Retinal ganglion cells responding selectively to direction and speed of image motion in the rabbit. J Physiol, 173(3), 377-407.

Barlow, H. B., Rosenblith, W. A. (1961). Possible principles underlying the transformations of sensory messages. In Sensory Communication (pp. 217-234). MIT Press.

Beraneck, M., and Cullen, K. E. (2007). Activity of vestibular nuclei neurons during vestibular and optokinetic stimulation in the alert mouse. J Neurophysiol, 98(3), 1549-1565.

Barry, J. M. (2015). Axonal activity in vivo: technical considerations and implications for the exploration of neural circuits in freely moving animals. Front Neurosci, 9, 153.

Bishop, P. O., Burke, W., Davis, R. (1962). The interpretation of the extracellular response of single lateral geniculate cells. J Physiol (Lond), 162, 451-472.

Bolz, J., Rosner, G., Wässle, H. (1982). Response latency of brisk-sustained (X) and brisk-transient (Y) cells in the cat retina. J Physiol, 328, 171-190.

Borghuis, B. G., Ratliff, C. P., Smith, R. G. (2018). Impact of light-adaptive mechanisms on mammalian retinal visual encoding at high light levels. J Neurophysiol, 119(4), 1437-1449.

Brown, R. E., Wong, A. A. (2007). The influence of visual ability on learning and memory performance in 13 strains of mice. Learn Mem, 14(3), 134-144.

Chang, L., He, S. (2014). Light adaptation increases response latency of alpha ganglion cells via a threshold-like nonlinearity. Neuroscience, 256, 101-116.

Chen, C., Song, S. (2019). Differential cell-type dependent brain state modulations of sensory representations in the non-lemniscal mouse inferior colliculus. Commun Biol, 2, 356.

Chichilnisky, E. J. (2001). A simple white noise analysis of neuronal light responses. Network, 12(2), 199-213.

Chichilnisky, E. J., Kalmar, R. S. (2002). Functional asymmetries in ON and OFF ganglion cells of primate retina. J Neurosci, 22(7), 2737-2747.

De Franceschi, G., Solomon, S. G. (2018). Visual response properties of neurons in the superficial layers of the superior colliculus of awake mouse. J Physiol, 596(24), 6307-6332.

Doi, E., Gauthier, J. L., Field, G. D., Shlens, J., Sher, A., Greschner, M., Machado, T. A., Jepson, L. H., Mathieson, K., Gunning, D. E., Litke, A. M., Paninski, L., Chichilnisky, E. J., Simoncelli, E. P. (2012). Efficient Coding of Spatial Information in the Primate Retina. J Neurosci, 32(46), 16256-16264.

Dombeck, D. A., Khabbaz, A. N., Collman, F., Adelman, T. L., Tank, D. W. (2007). Imaging large-scale neural activity with cellular resolution in awake, mobile mice. Neuron, 56(1), 43-57.

Durand, S., Iyer, R., Mizuseki, K., de Vries, S., Mihalas, S., Reid, R. C. (2016). A Comparison of Visual Response Properties in the Lateral Geniculate Nucleus and Primary Visual Cortex of Awake and Anesthetized Mice. J Neurosci, 36(48), 12133-12156.

Ellis, E. M., Gauvain, G., Sivyer, B., Murphy, G. J. (2016). Shared and distinct retinal input to the mouse superior colliculus and dorsal lateral geniculate nucleus. J Neurophysiol, 116(2), 602-610.

Enroth-Cugell, C., Robson, J. G. (1966). The contrast sensitivity of retinal ganglion cells of the cat. J Physiol, 187, 517-552.

Erisken, S., Vaiceliunaite, A., Jurjut, O., Fiorini, M., Katzner, S., Busse, L. (2014). Effects of locomotion extend throughout the mouse early visual system. Curr Biol, 24(24), 2899-2907.

Esposti, F., Johnston, J., Rosa, J. M., Leung, K.-M., Lagnado, L. (2013). Olfactory Stimulation Selectively Modulates the OFF Pathway in the Retina of Zebrafish. Neuron, 79(1), 97-110.

Franke, K., Chagas, A. M., Zhao, Z., Zimmermann, M. J., Bartel, P., Qiu, Y., Szatko, K. P., Baden, T., Euler, T. (2019). An arbitrary-spectrum spatial visual stimulator for vision research. Elife, 8, e48779.

Fuchs, A. F., Kimm, J. (1975). Unit activity in vestibular nucleus of the alert monkey during horizontal angular acceleration and eye movement. J Neurophysiol, 38(5), 1140-1161.

Gauvain, G., Murphy, G. J. (2015). Projection-specific characteristics of retinal input to the brain. J Neurosci, 35(16), 6575-6583.

Geng, Y., Dubra, A., Yin, L., Merigan, W. H., Sharma, R., Libby, R. T., Williams, D. R. (2012). Adaptive optics retinal imaging in the living mouse eye. Biomed Opt Express, 3(4), 715-734.

Gjorgjieva, J., Meister, M., Sompolinsky, H. (2019). Functional diversity among sensory neurons from efficient coding principles. PLoS Comput Biol, 15(11), e1007476.

Gollisch, T., Meister, M. (2008). Rapid neural coding in the retina with relative spike latencies. Science, 319(5866), 1108-1111.

Gollisch, T., Meister, M. (2010). Eye Smarter than Scientists Believed: Neural Computations in Circuits of the Retina. Neuron, 65, 150-164.

Greenberg, D. S., Houweling, A. R., Kerr, J. N. D. (2008). Population imaging of ongoing neuronal activity in the visual cortex of awake rats. Nat Neurosci, 11(7), 749-751.

Hagins, W. A., Penn, R. D., Yoshikami, S. (1970). Dark Current and Photocurrent in Retinal Rods. Biophys J, 10(5), 380-412.

Haider, B., Häusser, M., Carandini, M. (2013). Inhibition dominates sensory responses in the awake cortex. Nature, 493(7430), 97-100.

Hartline, H. K. (1938). The response of single optic nerve fibers of the vertebrate eye to illumination of the retina. Am J Physiol, 121, 400–415.

Hattar, S., Lucas, R. J., Mrosovsky, N., Thompson, S., Douglas, R. H., Hankins, M. W., Lem, J., Biel, M., Hofmann, F., Foster, R. G., Yau, K.-W. (2003). Melanopsin and rod-cone photoreceptive systems account for all major accessory visual functions in mice. Nature, 424(6944), 76-81

He, K., Gkioxari, G., Dollár, P., Girshick, R. (2017). Mask R-CNN. arXiv, 1703.06870.

Hong, G., Fu, T.-M., Qiao, M., Viveros, R. D., Yang, X., Zhou, T., Lee, J. M., Park, H.-G., Sanes, J. R. (2018). A method for single-neuron chronic recording from the retina in awake mice. Science, 360(6396), 1447-1451.

Jacobs, G. H., Williams, G. A. (2007). Contributions of the mouse UV photopigment to the ERG and to vision. Doc Ophthalmol, 115(3), 137-144.

1201 Jacoby, J., Schwartz, G. W. (2018). Typology and Circuitry of Suppressed-by-Contrast
1202 Retinal Ganglion Cells. Front Cell Neurosci, 12, 269.

1203 Jenkins, A., Franks, N. P., Lieb, W. R. (1999). Effects of temperature and volatile
1204 anesthetics on GABA(A) receptors. Anesthesiology, 90(2), 484-491.

1205 Jouty, J., Hilgen, G., Sernagor, E., Hennig, M. H. (2018). Non-parametric Physiological
1206 Classification of Retinal Ganglion Cells in the Mouse Retina. Front Cell Neurosci, 12, 481.

1207 Jun, J. J., Steinmetz, N. A., Siegle, J. H., Denman, D. J., Bauza, M., Barbarits, B., Lee, A.
1208 K., Anastassiou, C. A., Andrei, A., Aydın, Ç., Barbic, M., Blanche, T. J., Bonin, V., Couto,
1209 J., Dutta, B., Gratiy, S. L., Gutnisky, D. A., Häusser, M., Karsh, B., … Harris, T. D. (2017).
1210 Fully Integrated Silicon Probes for High-Density Recording of Neural Activity. Nature,
1211 551(7679), 232-236.

1212 Kaplan, E., Shapley, R. (1984). The origin of the S (slow) potential in the mammalian lateral
1213 geniculate nucleus. Exp Brain Res, 55(1), 111-116.

1214 Kasai, M., Isa, T. (2022). Effects of light isoflurane anesthesia on organization of direction
1215 and orientation selectivity in the superficial layer of the mouse superior colliculus. J
1216 Neurosci, 42(4), 619-630.

1217 Ke, J.-B., Wang, Y. V., Borghuis, B. G., Cembrowski, M. S., Riecke, H., Kath, W. L., Demb,
1218 J. B., Singer, J. H. (2014). Adaptation to background light enables contrast coding at rod
1219 bipolar cell synapses. Neuron, 81(2), 388-401.

1220 Krieger, B., Qiao, M., Rousso, D. L., Sanes, J. R., Meister, M. (2017). Four alpha ganglion
1221 cell types in mouse retina: Function, structure, and molecular signatures. PLoS One, 12(7),
1222 e0180091.

1223 Kuffler, S. W. (1953). Discharge patterns and functional organization of mammalian retina.
1224 J Neurophysiol, 16(1), 37-68.

1225 Laughlin, S. B. (2001). Energy as a constraint on the coding and processing of sensory
1226 information. Curr Opin Neurobiol, 11(4), 475-480.

1227 Lee, S.-H., Dan, Y. (2012). Neuromodulation of brain states. Neuron, 76(1), 209-222.

1228 Lettvin, J. Y., Maturana, H. R., McCulloch, W. S., Pitts, W. H. (1959). What the frog's eye
1229 tells the frog's brain. Proc Inst Radio Engr, 47, 1940-1951.

1230 Li, J. Y., Schmidt, T. M. (2018). Divergent projection patterns of M1 ipRGC subtypes. J
1231 Comp Neurol, 526(13), 2010-2018.

1232 Liang, L., Fratzl, A., Goldey, G., Ramesh, R. N., Sugden, A. U., Morgan, J. L., Chen, C.,
1233 Andermann, M. L. (2018). A Fine-Scale Functional Logic to Convergence from Retina to
1234 Thalamus. Cell, 173(6), 1343-1355.e24.

1235 Liang, L., Fratzl, A., Reggiani, J. D. S., Mansour, O. E., Chen, C., Andermann, M. L. (2020).
1236 Retinal Inputs to the Thalamus Are Selectively Gated by Arousal. Curr Biol, 30(20), 3923-
1237 3934.e9.

1238 Mani, A., Schwartz, G. W. (2017). Circuit Mechanisms of a Retinal Ganglion Cell with
1239 Stimulus-Dependent Response Latency and Activation Beyond Its Dendrites. Curr Biol,
1240 27(4), 471-482.

1241 Masland, R. H. (2012). The Neuronal Organization of the Retina. Neuron, 76, 266-280.

1242 Mastronarde, D. N. (1983). Correlated firing of cat retinal ganglion cells. I. Spontaneously
1243 active inputs to X- and Y-cells. J Neurophysiol, 49(2), 303-324.

1244 Mastronarde, D. N. (1985). Two types of cat retinal ganglion cells that are suppressed by
1245 contrast. Vision Res, 25(9), 1195-1196.

1246 Mazurek, M., Kager, M., van Hooser, S. D. (2014). Robust quantification of orientation
1247 selectivity and direction selectivity. Front Neural Circuits, 8, 92.

1248 Meister, M., Pine, J., Baylor, D. A. (1994). Multi-neuronal signals from the retina:
1249 acquisition and analysis. J Neurosci Methods, 51(1), 95-106.

1250 Miura, S. K., Scanziani, M. (2022). Distinguishing externally from saccade-induced motion
1251 in visual cortex. Nature, 610, 135-142.

1252 Molotkov, D., Ferrarese, L., Boissonnet, T., Asari, H. (2022) Topographic axonal projection
1253 at single-cell precision supports local retinotopy in the mouse superior colliculus. bioRxiv
1254 2022.03.25.485790.

1255 Niell, C. M., Stryker, M. P. (2010). Modulation of visual responses by behavioral state in
1256 mouse visual cortex. Neuron, 65(4), 472-479.

1257 Nikonov S. S., Kholodenko, R., Lem, J., Pugh, E. N. (2006). Physiological features of the
1258 S- and M-cone photoreceptors of wild-type mice from single-cell recordings. J Gen Physiol,
1259 127(4), 359-374.

1260 Nomura, Y., Ikuta, S., Yokota, S., Mita, J., Oikawa, M., Matsushima, H., Amano, A.,
1261 Shimonomura, K., Seya, Y., Koike, C. (2019). Evaluation of critical flicker-fusion frequency
1262 measurement methods using a touchscreen-based visual temporal discrimination task in
1263 the behaving mouse. Neurosci Res, 148, 28-33.

1264 Okawa, H., Sampath, A. P., Laughlin, S. B., Fain, G. L. (2008). ATP Consumption by
1265 Mammalian Rod Photoreceptors in Darkness and in Light. Curr Biol, 18(24), 1917-1921.

1266 Olshausen, B. A., Field, D. J. (1996). Emergence of simple-cell receptive field properties
1267 by learning a sparse code for natural images. Nature, 381(6538), 607-609.

1268 Pearson, J. T., Kerschensteiner, D. (2015). Ambient illumination switches contrast
1269 preference of specific retinal processing streams. J Neurophysiol, 114(1), 540-550.

1270 Pitkow, X., Meister, M. (2012). Decorrelation and efficient coding by retinal ganglion cells.
1271 Nat Neurosci, 15(4), 628-635.

Populin, L. C. (2005). Anesthetics Change the Excitation/Inhibition Balance That Governs Sensory Processing in the Cat Superior Colliculus. J Neurosci, 25(25), 5903-5914.

Ravi, S., Ahn, D., Greschner, M., Chichilnisky, E. J., Field, G. D. (2018). Pathway-Specific Asymmetries between ON and OFF Visual Signals. J Neurosci, 38(45), 9728-9740.

Raz, A., Grady, S. M., Krause, B. M., Uhlrich, D. J., Manning, K. A., Banks, M. I. (2014). Preferential effect of isoflurane on top-down vs. bottom-up pathways in sensory cortex. Front Syst Neurosci, 8, 191.

Repérant, J., Ward, R., Miceli, D., Rio, J. P., Médina, M., Kenigfest, N. B., Vesselkin, N. P. (2006). The centrifugal visual system of vertebrates: a comparative analysis of its functional anatomical organization. Brain Res Rev, 52(1), 1-57.

Rhode, W. S., and Smith, P. H. (1986). Encoding timing and intensity in the ventral cochlear nucleus of the cat. J Neurophysiol, 56(2), 261-286.

Rieke, F., Warland, D., Van Steveninck, R. D. R., Bialek, W. (1997). Spikes: Exploring the Neural Code. MIT Press. ISBN: 9780262681087.

Rosón, M.R., Bauer, Y., Kotkat, A. H., Berens, P., Euler, T., Busse, L. (2019). Mouse dLGN Receives Functional Input from a Diverse Population of Retinal Ganglion Cells with Limited Convergence. Neuron, 102(2), 462-476.e8.

Rossant, C. (2020). Phy: interactive visualization and manual spike sorting of large-scale ephys data. GitHub. https://github.com/cortex-lab/phy

Sachs, M. B., Abbas, P. J. (1974). Rate versus level functions for auditory-nerve fibers in cats: tone-burst stimuli. J Acoust Soc Am, 56(6), 1835-1847.

Sagdullaev, B. T., McCall, M. A. (2005). Stimulus size and intensity alter fundamental receptive-field properties of mouse retinal ganglion cells in vivo. Vis Neurosci, 22(5), 649-659.

Samonds, J. M., Geisler, W. S., Priebe, N. J. (2018). Natural image and receptive field statistics predict saccade sizes. Nat Neurosci, 21, 1591-1599.

Sanes, J. R., Masland, R. H. (2015). The types of retinal ganglion cells: current status and implications for neuronal classification. Annu Rev Neurosci, 38, 221-246.

Schröder, S., Steinmetz, N. A., Krumin, M., Pachitariu, M., Rizzi, M., Lagnado, L., Harris, K. D., Carandini, M. (2020). Arousal Modulates Retinal Output. Neuron, 107(3), 487-495.

Schwartz, G.W. (2021). Retinal Computation. Academic Press. ISBN: 9780128198964.

Sellers, K. K., Bennett, D. V., Hutt, A., Williams, J. H., Fröhlich, F. (2015). Awake vs. anesthetized: layer-specific sensory processing in visual cortex and functional connectivity between cortical areas. J Neurophysiol, 113(10), 3798-3815.

Shekhar, K., Lapan, S. W., Whitney, I. E., Tran, N. M., Macosko, E. Z., Kowalczyk, M., Adiconis, X., Levin, J. Z., Nemesh, J., Goldman, M., McCarroll, S. A., Cepko, C. L., Regev, A., Sanes, J. R. (2016). Comprehensive Classification of Retinal Bipolar Neurons by Single-Cell Transcriptomics. Cell, 166(5), 1308-1323.e30.

Sibille, J., Gehr, C., Benichov, J. I., Balasubramanian, H., Teh, K. L., Lupashina, T., Vallentin, D., Kremkow, J. (2022). High-density electrode recordings reveal strong and specific connections between retinal ganglion cells and midbrain neurons. Nat Commun, 13, 5218.

Smeds, L., Takeshita, D., Turunen, T., Tiihonen, J., Westö, J., Martyniuk, N., Seppänen, A., Ala-Laurila, P. (2019). Paradoxical Rules of Spike Train Decoding Revealed at the Sensitivity Limit of Vision. Neuron, 104(3), 576-587.e11.

Strauss, O. (2005). The retinal pigment epithelium in visual function. Physiol Rev, 85(3), 845-881.

Tengölics, Á. J., Szarka, G., Ganczer, A., Szabó-Meleg, E., Nyitrai, M., Kovács-Öller, T., Völgyi, B. (2019). Response Latency Tuning by Retinal Circuits Modulates Signal Efficiency. Sci Rep, 9(1), 15110.

Ter-Mikaelian, M., Sanes, D. H., Semple, M. N. (2007). Transformation of temporal properties between auditory midbrain and cortex in the awake Mongolian gerbil. J Neurosci, 27(23), 6091-6102.

Tien, N.-W., Pearson, J. T., Heller, C. R., Demas, J., Daniel, K. (2015). Genetically Identified Suppressed-by-Contrast Retinal Ganglion Cells Reliably Signal Self-Generated Visual Stimuli. J Neurosci, 35(30), 10815-10820.

Tikidji-Hamburyan, A., Reinhard, K., Seitter, H., Hovhannisyan, A., Procyk, C. A., Allen, A. E., Schenk, M., Lucas, R. J., Münch, T. A. (2015). Retinal output changes qualitatively with every change in ambient illuminance. Nat Neurosci, 18(1), 66-74.

Umino, Y., Pasquale, R., Solessio, E. (2018). Visual Temporal Contrast Sensitivity in the Behaving Mouse Shares Fundamental Properties with Human Psychophysics. eNeuro, 5(4), ENEURO.0181-18.2018.

Vaiceliunaite, A., Erisken, S., Franzen, F., Katzner, S., Busse, L. (2013). Spatial integration in mouse primary visual cortex. J Neurophysiol, 110(4), 964-972.

van Wyk, M., Wässle, H., Taylor, W. R. (2009). Receptive field properties of ON- and OFF-ganglion cells in the mouse retina. Vis Neurosci, 26(3), 297-308.

Vidal-Sanz, M., Galindo-Romero, C., Valiente-Soriano, F. J., Nadal-Nicolás, F. M., Ortin-Martinez, A., Rovere, G., Salinas-Navarro, M., Lucas-Ruiz, F., Sanchez-Migallon, M. C., Sobrado-Calvo, P., Aviles-Trigueros, M., Villegas-Pérez, M. P., Agudo-Barriuso, M. (2017). Shared and Differential Retinal Responses against Optic Nerve Injury and Ocular Hypertension. Front Neurosci, 11, 235.

Vlasiuk, A., Asari, H. (2021). Feedback from retinal ganglion cells to the inner retina. PLoS One, 16(7), e0254611.

Vogel, B., Wagner, H., Gmoser, J., Wörner, A., Löschberger, A., Peters, L., Frey, A., Hofmann, U., Frantz, S. (2016). Touch-free measurement of body temperature using close-up thermography of the ocular surface. MethodsX, 3, 407-416.

Wang, X., Chen, C., Zhang, D., Yao, H. (2014). Cumulative latency advance underlies fast visual processing in desynchronized brain state. Proc Natl Acad Sci USA, 111(1), 515-520.

Wang, Y. V., Weick, M., Demb, J. B. (2011). Spectral and temporal sensitivity of cone-mediated responses in mouse retinal ganglion cells. J Neurosci, 31(21), 7670-7681.

Warchol, M. E., Dallos, P. (1990). Neural coding in the chick cochlear nucleus. J Comp Physiol A, 166(5), 721-734.

Warland, D. K., Reinagel, P., Meister, M. (1997). Decoding visual information from a population of retinal ganglion cells. J Neurophysiol, 78(5), 2336-2350.

Warwick, R. A., Kaushansky, N., Sarid, N., Golan, A., Rivlin-Etzion, M. (2018). Inhomogeneous Encoding of the Visual Field in the Mouse Retina. Curr Biol, 28(5), 655-665.e3.

Weyand, T. G. (2007). Retinogeniculate transmission in wakefulness. J Neurophysiol, 98(2), 769-785.

Wright, P. W., Brier, L. M., Bauer, A. Q., Baxter, G. A., Kraft, A. W., Reisman, M. D., Bice, A. R., Snyder, A. Z., Lee, J.-M., Culver, J. P. (2017). Functional connectivity structure of cortical calcium dynamics in anesthetized and awake mice. PLoS One, 12(10), e0185759.

Wu, J. S., Young, E. D., Glowatzki, E. (2016). Maturation of Spontaneous Firing Properties after Hearing Onset in Rat Auditory Nerve Fibers: Spontaneous Rates, Refractoriness, and Interfiber Correlations. J Neurosci, 36(41), 10584-10597.

1367 Yan, W., Laboulaye, M. A., Tran, N. M., Whitney, I. E., Benhar, I., Sanes, J. R. (2020).
1368 Mouse Retinal Cell Atlas: Molecular Identification of over Sixty Amacrine Cell Types. J
1369 Neurosci, 40(27), 5177-5195.

1370 Yger, P., Spampinato, G. L., Esposito, E., Lefebvre, B., Deny, S., Gardella, C., Stimberg,
1371 M., Jetter, F., Zeck, G., Picaud, S., Duebel, J., Marre, O. (2018). A spike sorting toolbox
1372 for up to thousands of electrodes validated with ground truth recordings in vitro and in vivo.
1373 Elife, 7, e34518.

1374 Yin, L., Geng, Y., Osakada, F., Sharma, R., Cetin, A. H., Callaway, E. M., Williams, D. R.,
1375 Merigan, W. H. (2013). Imaging light responses of retinal ganglion cells in the living mouse
1376 eye. J Neurophysiol, 109(9), 2415-2421.

1377 Yin, L., Masella, B., Dalkara, D., Zhang, J., Flannery, J. G., Schaffer, D. V., Williams, D.
1378 R., Merigan, W. H. (2014). Imaging light responses of foveal ganglion cells in the living
1379 macaque eye. J Neurosci, 34(19), 6596-6605.

1380 Yonehara, K., Ishikane, H., Sakuta, H., Shintani, T., Nakamura-Yonehara, K., Kamiji, N.
1381 L., Usui, S., Noda, M. (2009). Identification of retinal ganglion cells and their projections
1382 involved in central transmission of information about upward and downward image motion.
1383 PLoS One, 4(1), e4320.

1384 Zaghloul, K. A., Boahen, K., Demb, J. B. (2003). Different circuits for ON and OFF retinal
1385 ganglion cells cause different contrast sensitivities. J Neurosci, 23(7), 2645-2654.

1386 Zhang, Y., Kim, I.-J., Sanes, J. R., Meister, M. (2012). The most numerous ganglion cell
1387 type of the mouse retina is a selective feature detector. Proc Natl Acad Sci U S A, 109(36),
1388 E2391-E2398.

1389 Zhao, X., Liu, M., Cang, J. (2014). Visual cortex modulates the magnitude but not the
1390 selectivity of looming-evoked responses in the superior colliculus of awake mice. Neuron,
1391 84(1), 202-213.

Zohar, O., Shackleton, T. M., Nelken, I., Palmer, A. R., Shamir, M. (2011). First spike latency code for interaural phase difference discrimination in the guinea pig inferior colliculus. J Neurosci, 31(25), 9192-9204.